



Mode I delamination R-curve in poplar laminated veneer lumber

Axel Peignon, Joël Serra, L. Gélard, Arthur Cantarel, Florent Eyma, B. Castanié

► To cite this version:

Axel Peignon, Joël Serra, L. Gélard, Arthur Cantarel, Florent Eyma, et al.. Mode I delamination R-curve in poplar laminated veneer lumber. Theoretical and Applied Fracture Mechanics, 2023, 126, pp.103982. 10.1016/j.tafmec.2023.103982 . hal-04141431v1

HAL Id: hal-04141431

<https://hal.science/hal-04141431v1>

Submitted on 26 Jun 2023 (v1), last revised 25 Aug 2023 (v2)

HAL is a multi-disciplinary open access archive for the deposit and dissemination of scientific research documents, whether they are published or not. The documents may come from teaching and research institutions in France or abroad, or from public or private research centers.

L'archive ouverte pluridisciplinaire **HAL**, est destinée au dépôt et à la diffusion de documents scientifiques de niveau recherche, publiés ou non, émanant des établissements d'enseignement et de recherche français ou étrangers, des laboratoires publics ou privés.

Mode I delamination R-Curve in poplar laminated veneer lumber

A. Peignon, J. Serra, L. Gélard, A. Cantarel, F. Eyma, B. Castanié

PII: S0167-8442(23)00245-8

DOI: <https://doi.org/10.1016/j.tafmec.2023.103982>

Reference: TAFMEC 103982

To appear in: *Theoretical and Applied Fracture Mechanics*

Received Date: 7 February 2023

Revised Date: 15 June 2023

Accepted Date: 15 June 2023



Please cite this article as: A. Peignon, J. Serra, L. Gélard, A. Cantarel, F. Eyma, B. Castanié, Mode I delamination R-Curve in poplar laminated veneer lumber, *Theoretical and Applied Fracture Mechanics* (2023), doi: <https://doi.org/10.1016/j.tafmec.2023.103982>

This is a PDF file of an article that has undergone enhancements after acceptance, such as the addition of a cover page and metadata, and formatting for readability, but it is not yet the definitive version of record. This version will undergo additional copyediting, typesetting and review before it is published in its final form, but we are providing this version to give early visibility of the article. Please note that, during the production process, errors may be discovered which could affect the content, and all legal disclaimers that apply to the journal pertain.

Mode I delamination R-Curve in poplar laminated veneer lumber

A. Peignon¹, J. Serra¹, L. Gélard¹, A. Cantarel¹, F. Eyma¹ and B. Castanié^{1,*}

¹ Institut Clément (ICA), Université de Toulouse, CNRS UMR 5312, INSA, ISAE-Supaéro, INSA, IMT Mines Albi, UPS, Toulouse, France

*corresponding author: bruno.castanie@insa-toulouse.fr

Abstract: Recent studies have shown that plywood and laminated veneer lumber are very efficient crashworthiness materials. Therefore, there is a need to determine the fracture toughness of these wood composite materials to be able to model their static and dynamic damage behavior. This study reports the results of the delamination propagation of plywood under mode I loading. Two different double cantilever beam specimens made of poplar were compared: one with an interfacial fiber orientation of 0°/0° and the second with 0°/90°. Failure scenarios and patterns are analyzed to establish a comparison between the two configurations and compute consistent R-curves.

Keywords: Wood veneers, R-curve, Double Cantilever Beam (DCB), Delamination, Fiber bridging, Laminated veneer lumber (LVL)

Funding: This work was supported by the French National Research Agency under the BOOST project (ANR-21-CE43-0008-01).

CC: Compliance Calibration
DCB: Double Cantilever Beam
IR: InfraRed
LVL: Laminated Veneer Lumber
MBT: Modified Beam Theory
MCC: Modified Compliance Calibration
RSD: Relative Standard Deviation
SEA: Specific Energy Absorption
SD: Standard Deviation

Nomenclature

a	crack length
a_0	initial crack length
b	specimen width
C	specimen compliance
E_L	modulus of elasticity of wood along the longitudinal direction
G_{Ic}	fracture toughness in mode I
h	specimen height
I	moment of inertia of a DCB specimen arm
L	veneer longitudinal direction
L'	half width of loading block
l	specimen length
P	load acting on the specimen
R	veneer Radial direction
T	veneer Tangential direction
t	distance from loading block pin to center line of top specimen arm
X	specimen length direction
x_0	x coordinate of the crack origin
x_1	x coordinate of point 1
x_f	x coordinate of crack tip
Y	specimen depth direction
y_0	y coordinate of crack origin
y_1	y coordinate of point 1
y_f	y coordinate of crack tip
Z	specimen thickness direction
δ	applied displacement
λ_i	i-th coefficient of an unknown function

1. Introduction

Wood is one of the earliest materials used by man in construction [1]. It is a well-known material for which there exists fairly detailed knowledge of its pathologies and durability characteristics. One of the first building codes concerned wood as the material and was published in 1091 in China [2].

Wood, especially used in sandwich structures, was also one of the materials used in aeronautics in its early days and until the Second World War [3]. In addition, it is a natural and renewable material, which can be produced locally and recycled [4], [5]. It also acts as a carbon sink, a natural reservoir capable of absorbing and storing carbon from atmospheric CO₂. Wood can therefore play a key role in the fight against global warming [6]. Its waste products are also reusable as a secondary material or energy source [7] and structural material [8].

Laminated veneer lumber (LVL) and plywood are structural composite products made from thin, peeled wood plies, called veneers, assembled with an adhesive. Plywood has cross-lamination, which means that longitudinal and transverse veneers are alternated throughout the laminate [9]. Because of their manufacturing steps, LVL and plywood offer the possibility of selecting veneers without visible defects such as knots, knotholes or cracks and have static mechanical characteristics comparable to, or even superior to, those of solid wood [10]–[13]. In addition, recent studies by the authors have shown that LVL also has interesting mechanical potential for crash or impact applications [14]–[18]. For example, Guélou et al. [14] obtained a dynamic Specific Energy Absorption (SEA) for birch wood ranging between 35.7 J/g and 41.1 J/g. The SEA refers to the amount of energy per gram that a material can absorb before it fails or breaks. In addition, sandwich structures with plywood cores and composite (glass, carbon, linen) or metal (aluminium) skins [19], have shown very good resistance to low-speed/low-energy impact [20] as well as excellent post-impact compressive strength in configurations with aluminium skin and linen, where the knockdown factor is less than 10% [15].

However, a previous study simulated impact on wood based materials with a damage law available in LS-Dyna [21]. This study showed a deficiency of this type of approach. Additionally, based on their experience of the impact on composite structures [22]–[25] the authors believe that the use of the so-called Discrete Ply Model [23]–[25] modeling strategy would be relevant to model the fracture

scenarios of plywood-based structures, in both static and dynamic situations. This strategy is based on only 13 parameters, including energy fracture toughness at interfaces, which should be identified specifically for wood applications.

To characterize the glue joint, the standard NF EN 302 (AFNOR 2017) or the former standard DIN 53253 (DIN 1964) propose to test the shear strength of the glue joint via longitudinal tensile tests. However, during this type of test, only the strength of the glue line is characterized [26]. Thus, synthetic composite materials standard ASTM D5528 (ASTM 2010) is considered to characterize the toughness of a glued interface in mode I. This opening mode is studied as a priority because, in general among the three modes of propagation of a crack, it is the one that requires the least energy and is therefore the most dangerous for the structure. The mode I toughness of the LVL is generally characterized by a DCB (Double Cantilever Beam) test. This test makes it possible to obtain the Resistance curve of the characterized interface, also called the R-curve. This curve represents the amount of energy required to propagate an initial crack in the interface to be characterized [27]. The few authors who have shown interest in DCB tests on glued wood interfaces, either for LVL or plywood include El Moustaphaoui et al. [28], [29], who characterized the toughness of a 9-ply ceiba plywood interface, without specifying its stacking sequence, using urea-formaldehyde glue. They obtained a G_{Ic} value between 140 J/m² and 200 J/m². Baba et al. [30] were interested in the delamination of beech plywood with a 0°/0° interface and the stacking sequence [0°/90°/0°]_s. They obtained a G_{Ic} value of the order of 20 J/m². This value, which is low compared to that of El Moustaphaoui, can be explained by the addition of rye flour in the urea-formaldehyde glue used to make the test tubes. Other authors have been interested in glued wood interfaces in glulam [31]–[37]. The order of magnitude of G_{Ic} values obtained by these studies is a few hundred Joules per square meters.

Previous studies only considered 0°/0° delamination interfaces [28]–[37] but, in the case of laminates such as plywood, delamination occurs mainly at 0°/90° interfaces because interlaminar shear is maximum for perpendicularly oriented interfaces. This phenomenon is well known in the field of composites [38] but not studied for wood.

In the case of laminates made of synthetic composite materials, the configuration with a $0^\circ/0^\circ$ interface makes it possible to find a lower bound for the value of G_{Ic} by limiting fiber bridging while keeping the crack in the interface between the $0^\circ/0^\circ$ plies. The configuration with a $0^\circ/90^\circ$ interface is more likely to create migration of the crack into the 90° ply and therefore will tend to overestimate the G_{Ic} [39], [40].

Moreover, in the case of LVL or plywood, only El Moustaphaoui et al. have computed R-curves [28]. Baba et al. have reproduced an R-curve characterizing the G_{Ic} of initiation for various initial cracks [30]. However, once the R-curve is obtained, few physical justifications are provided to explain its evolution and analyze these specimens' fracture surfaces.

Therefore, the study presented here aims to provide mode I delamination R-curves for two different interfaces: a $0^\circ/0^\circ$ interface and a $0^\circ/90^\circ$ interface. The evolution of the R-curve will be analyzed for Koster poplar (*Populus*) plywood and a comparison will be made between the two interfaces studied. The corresponding fracture toughness will be calculated and analyzed.

2. Materials and Experimental Procedures

The Double Cantilever Beam (DCB) test consists of applying a load to the ends of the specimen, which causes the crack to propagate in pure mode I. The specimen is placed with an initial crack length (a_0). Figure 1 shows the DCB test and the depiction of the initial crack. The fracture energy can be evaluated using the force-displacement curve (P - δ curve), the crack length (a), and the Irwin-Kies equation [41] (Equation 1):

$$G_{Ic} = \frac{P^2 dC}{2bda}$$

Equation 1

with b as the width of the specimen and C as the compliance of the specimen (Equation 2).

$$C = \frac{\delta}{P}$$

Equation 2

2.1. Materials and Manufacturing

One-millimeter Koster wood veneers were used in the manufacture of the DCB test specimens. The veneer, supplied by the LaBoMaP laboratory in Cluny, France, was produced using a rotary wood peeling machine. The moisture content of the wood was measured at 10.1% with a Relative Standard Deviation (RSD) of 0.4%. The veneers were then stacked and pressed for 5 hours at 10 bars and 25°C. The wood glue used to make the plywood was Kleiberit PUR 510 FIBERBOND, a one-component polyurethane-based glue that hardens by reaction with moisture. The amount of glue used was 250 g/m². The density of Koster veneers was 348 kg/m³ (RSD: 4%).

Two specimen configurations were made for this study and are illustrated in Figure 2:

- 8-ply laminates with a $[0^\circ]_8$ stacking sequence to study the $0^\circ/0^\circ$ interface, referred to as “ $0^\circ/0^\circ$ specimens”.
- 9-ply laminates with a $[0^\circ_4, 90^\circ, 0^\circ_4]$ stacking sequence to study the $0^\circ/90^\circ$ interface, referred to as “ $0^\circ/90^\circ$ specimens”. A view of the thickness is shown in Figure 3.

Two reference frames will be used to describe the systems (Figure 3):

- A global reference frame (X,Y,Z) with X oriented along the length of the DCB specimen, Y in its depth, and Z in its thickness (Figure 1).
- A local reference frame (L,T,R), describing the main directions of the wood, is used to characterize the veneers (L oriented in the direction of the wood fibers (the wood cells), R oriented in the direction of the growth rings, and so in the thickness of the veneers, and T in the transverse direction in the plane of the veneers).

It is important to note that, during the manufacture of veneers, lathe checks are created on one of their faces [42], [43]. Lathe checks are small cracks (~ 0.1 mm in the veneer used for this study) that occur along the length of the veneer layers in plywood (Figure 4). These cracks happen when the veneer is manufactured (Figure 5). In addition, the thickness of a wood veneer can be composed of earlywood (wood formed at the beginning of the growing season) and latewood (wood formed later in the season) [44] (Figure 5). It is important to note that the anatomy and the mechanical properties of those two kinds of wood are different [45]–[47].

Moreover, unlike carbon composite materials, in wood, and so veneers, not all wood fibers are perfectly aligned, they may have an in-plane and an out-of-plane angle. This is due to the wood nature and, for veneers, the manufacturing process. Since the out-of-plane angle is mainly due to the irregularity of the wood log, when the veneer is peeled, the fibers in the LR plane of the veneer are not aligned with the L direction (Figure 6).

The plywood manufactured for the DCB specimen considers the positions of the lathe checks present in the Koster veneer. During stacking, faces with lathe checks are placed on healthy faces, except for the outer plies, where the cracked faces face the inside of the plywood. This stack is called “tight side out and loose side in” and it is this setup that is used in industry for the manufacture of plywood [48]. Figure 7 illustrates the stack used for $0^\circ/0^\circ$ specimens.

For the $0^\circ/90^\circ$ interfacial orientation, it was therefore decided to orient the cracked face of the 0° ply towards the inside of the interface. Figure 8 illustrates the location of the lathe checks at the $0^\circ/90^\circ$ interface in the XZ and YZ planes.

A total of 12 specimens per configuration were laser cut. DCB specimens had nominal dimensions of $250(l) \times 25(b) \times 8(h)$ mm³ for the $0^\circ/0^\circ$ series and $250(l) \times 25(b) \times 9(h)$ mm³ for the $0^\circ/90^\circ$ series (shown in Figure 9). Attachment blocks were chosen to attach the DCB specimens to the tension machine. The initial notch (a_0) was made in two stages: a Teflon film was placed during the production of the plywood (as recommended by ASTM D5528 (ASTM 2010)), and then the crack was initiated using a thin cutter blade. The insertion of the cutter blade made it possible to spread the arms slightly so that cracking was initiated without damaging the crack tip. The initiation made with the cutter reduced the variability related to a possible glue cluster at the end of the Teflon film.

2.2. Experimental Setup

DCB tests were performed at ambient temperature and humidity (23.5°C (SD: 0.5°C) and 47% H (SD: 2% H)). An Instron 5900 machine was used to perform the tests using a displacement control (Figure 10). A 50 kN force cell was installed, with a measurement accuracy of 0.5 N, and the travel speed was set at 20 mm/min.

Digital Image Correlation (DIC) was used to track sample deformation. A 5 MP camera (2452x2052 pixels) was used to acquire images of the specimens during the test. An infrared thermography (IRT) camera (M3K - Telops) was placed on the other side of the specimens to examine the propagation of damage during the test. The specimens were painted with matt black paint on one side for the IRT camera, to have a constant and maximum emissivity, and with speckles on the other side for image correlation (Figure 10). The speckles were made using spray paint and the size of the patterns was determined according to the experimental configuration to obtain a minimum size of 3 pixels for each speckle [49].

A data acquisition system was used to record both the applied load (P) and the vertical displacement of the clamps (δ) (Figure 1), with the acquisition frequency related to image correlation set at 1 Hz.

Image correlation data were analyzed with VIC 2D® correlation software. Calibration was carried out using a calibration pattern. The acquisition frequency of the thermal imaging camera was set at 50 Hz.

2.3. Methodology

To compute the fracture energy with a DCB test and the methods presented in ASTM D5528 (ASTM 2010), it is necessary to establish a link between compliance C and crack length to obtain dC/da (Equation 1). Many models are documented in the literature, the main ones being:

- Compliance Calibration (CC) ($C = \lambda_0 a^{\lambda_1}$; λ_0 and λ_1 are constants that need to be identified), described in ISO 15024 (ISO 2001) and ASTM D5528 (ASTM 2010),
- Modified Compliance Calibration (MCC) ($C^{1/3} = \lambda_1 a/h + \lambda_0$; λ_0 and λ_1 are constants that need to be identified), described in ASTM D5528 (ASTM 2010),
- Modified Beam Theory (MBT) ($C = 2a^3/3E_I I$) described in ISO 15024 (ISO 2001) and ASTM D5528 (ASTM 2010).

DIC was used to obtain the crack length required in the three methods employed in this paper. To post-process DIC images, the size of the subset was fixed so that the subset contained 3 to 4 speckles. The confidence interval of the correlation (called "Sigma") was used to visualize the correlation mismatch and thus estimate the position of the crack tip of the specimens (Figure 11). The Sigma cut-

off value chosen was 0.015, which corresponds to the maximum value obtained when calculating the confidence interval between two identical images. The value obtained corresponded to the noise in the study area, so values below 0.015 will not be considered hereafter and are, therefore, not related to the presence of a crack. In addition, the resolution of the camera was 4.55 pixels for 1 mm; so, a correlation confidence interval of 0.015 pixels corresponds to an interval of 0.0033 mm.

A Python script was used to track the crack tip using Sigma visualization obtained for each specimen over time. Manual point-by-point monitoring was carried out to obtain the coordinates in millimeters of the tip of the crack at each time.

When setting up DIC cameras, a compromise was used to see as many of the samples as possible while keeping a resolution high enough to allow sufficient resolution of the speckles. Therefore, the ends of the specimens were not visible during the test. That is why to obtain the crack length, it is necessary to compute it by using the origin of the crack and consider the bending of the lower arm of all the specimens during the tensile test. For each image captured, three points were tracked and used for specimen curvature interpolation. The first point corresponded to the crack tip (x_f, y_f) , the second to the origin of the crack (x_0, y_0) , and the third was taken on the interface of the specimen between the first and second points (x_1, y_1) , (Figure 12). A second-order function was used to fit this set of points (named $f(x)$). Then, the length of the crack was calculated between the origin of the crack and the crack tip with Equation 3 for each image:

$$a = \int_{x_0}^{x_f} \sqrt{1 + f'(x)^2} dx$$

Equation 3

To validate the method implemented, the measured and calculated lengths of the initial crack were compared for each specimen. Figure 13 illustrates the difference between these two values for all DCB specimens. The average deviation of this difference is 0.33 mm. The accuracy of ½ mm recommended by the ASTM D5528 standard (ASTM 2010) was thus respected.

3. Results

Once the tests were completed, each specimen was inspected to remove specimens with "abnormal" fracture patterns from the study. For example, in some $0^\circ/0^\circ$ series specimens, the crack migrated into the plies at the beginning of the test even though it was initially at the interface. Since the force applied was no longer symmetrical, the crack propagation was no longer in pure mode I and these DCB tests were, therefore, no longer considered valid. For this reason, four specimens were excluded from this study. This migration of the crack in the $0^\circ/0^\circ$ configuration can be explained by the out-of-plane variation of the grain angle in the veneers (Figure 14 and Figure 15), not all wood fibers are horizontal and they may have an out-of-plane angle. This phenomenon is not common in DCB tests of composite composites [50]. In addition, as explained in §2.3, the end of the specimen was not visible, and monitoring the crack-tips coordinates (x_f , y_f) was no longer possible for the last propagations and the final fracture, so the last crack propagation leading to the final rupture of the specimen was not considered in this study.

The P - δ curves obtained during the tests, keeping only viable specimens, are shown by series in Figure 16. On the $0^\circ/90^\circ$ specimens, no anomaly is found during the tests, all the specimens can be used.

There is already a greater variability for the $0^\circ/0^\circ$ series compared to the $0^\circ/90^\circ$ series.

3.1. R-curves

For the sake of clarity, only the fracture toughness and R-curves computed with the MCC method will be presented and illustrated in this sub-section.

A criterion for estimating repeatability during a DCB test campaign was the variability of the interpolation coefficients determined to correlate compliance and crack length. It is recalled that the MCC method uses an interpolation of $\log(C)$ with $\log(a)$. The fitted curves are shown in Figure 17. The $0^\circ/90^\circ$ series has a lower regression curve slope variability compared to $0^\circ/0^\circ$ series. This lower variability is consistent with the variability observed on the P - δ curves (Figure 16). Note that the average R^2 obtained for all fitting curves is 0.988 (SD: 0.011).

The first part of crack propagation, corresponding to the initiation of delamination, i.e. first G_{Ic} values, were not considered in this study, in accordance with ASTM D5528 (ASTM 2010). G_{Ic} values were

calculated only once the measured force had reached its maximum value and then decreased by 5%.

The R-curves obtained by the MCC method are shown in Figure 18.

The values for all the test specimens reported in Figure 18 shows that the average value of G_{Ic} is higher for the $0^\circ/0^\circ$ specimens than for the $0^\circ/90^\circ$ ones. This difference is related to the difference of the amount of fiber-bridging. $0^\circ/0^\circ$ specimens exhibited larger amount of fiber-bridging than $0^\circ/90^\circ$ ones. To validate this observation, the IR images obtained during the tests were subtracted one by one to obtain the heating between each image. It was thus understood that the heating observed did not come from the background, but from a self-heating in the specimen, related to a dissipation of energy (fiber failure - Figure 19). The IR imagery provides a visualization of irreversible energy dissipation through temperature variations. This self-heating, of the order of 1°C confirmed the presence of fiber rupture, which can be observed in the post-mortem specimens of Figure 19. This variation of energy is associated with fiber rupture because it is a phenomenon more energetic than decohesion alone [51], and it was not throughout the whole test. Fiber bridging is more common in wood than in conventional composites because the variability in the out-of-plane angle of the fibers is much higher than that encountered in carbon composites [52].

In addition, there is a tendency for $0^\circ/0^\circ$ ply G_{Ic} to increase throughout propagation. This has however only been observed on a single specimen. The authors believe that this phenomenon cannot be clearly identified in the others because the valid crack propagation (without ply failure or crack migration) is too small. Fiber bridging is a two-step phenomenon: first fibers are being slowly pulled out and then they are broken. That increase in force needed to break the fibers is the reason for the increase in computed G_{Ic} . For the other specimens only the first part of the fiber bridging (fiber pull-out) is observed. It has to be noted that for DCB tests on solid wood, during the fiber bridging, there are as many fibers that break as fibers that bridge in the LT plane [53]. Fiber bridging is therefore a lot more constant throughout crack propagation. In the present study, it seems that the low stiffness of the arms of the DCB specimens made the pulled-out fibers break later.

As for the $0^\circ/90^\circ$ series, the G_{Ic} remains quasi-constant, slightly decreasing, when the crack propagates in the specimen. This can be explained by the fact that a lot less fiber bridging occurs in the

0°/90° specimens. There was therefore a much greater variability in the 0°/0° specimens. The average values of fracture toughness obtained were: $G_{Ic-0°/0°} = 422 \text{ J/m}^2$ (RSD: 30%) and $G_{Ic-0°/90°} = 247 \text{ J/m}^2$ (RSD: 21%). However, once the measured force reaches its maximum value and then decreases by 5%, the average initial G_{Ic} , as defined in ASTM D5528 (ASTM 2010), is similar between the 0°/0° specimens and the 0°/90° specimens.

To ensure that the potential error from the method used here to track the crack did not have a significant effect on the calculated G_{Ic} values, the G_{Ic} curves obtained were compared with curves obtained by adding artificial random noise on the measured crack lengths. By adding a random measurement error of $\pm 1.5 \text{ mm}$ (a value higher than the maximum error observed in Figure 13), a maximum deviation of 1.75% was measured between the G_{Ic} curves (Figure 20). The method used to calculate G_{Ic} seems to be robust and the potential deviations of the crack length measurements do not disturb the calculated values.

In this sub-section, only the MCC method has been used to compute G_{Ic} . However, the results obtained with the two other methods presented (CC and MBT) differed with some specimens. Another method based on beam theory that does not require the use of the crack length can also be used to compute G_{Ic} with Equation 4 [54]:

$$G_{Ic} = \frac{3\delta P}{2b} \times \left(\frac{2}{E_I C} \right)^{1/3}$$

Equation 4

The four methods were compared for each specimen. Figure 21 illustrates the relative deviation between the MCC method and the other three methods. The comparison between the 4 methods on the 0°/0° specimens shows large differences in half of the specimens. On 0°/90° specimens, there are significant differences only on a small number of specimens. However, there is little difference between the CC and MCC methods, and similarly between the MBT and beam theory methods. The small difference between the MBT method and the beam theory method is reassuring regarding crack tracking. The differences between on one side the methods based on beam theory (MBT and beam theory method) and on the other side the CC and MCC methods can be explained by the presence of

fiber bridging for the $0^\circ/0^\circ$ specimens and the presence of fiber bridging in the 90° ply for the $0^\circ/90^\circ$ specimens. Methods based on beam theory considered perfect beams without the presence of fiber bridging, on the other hand, CC and MCC methods are calibrated with compliance as a function of the crack length, and so, offer more flexibility and indirectly consider the effect of fiber bridging.

However, the relative deviation between the mean G_{Ic} for the $0^\circ/90^\circ$ specimens, computed with the MCC method and the MBT method, differed by only 7.5%. This relative deviation is comparable to that obtained by El Moustaphaoui et al. in Ceiba plywood [29]. Also, for the $0^\circ/0^\circ$ specimens, this relative deviation is 21%. The rest of this paper will use the MCC method, as it, with the CC method, is the one that needs the weakest assumptions about the relationship between compliance and crack length. Furthermore, this method provides R^2 coefficients closer to 1 on the calibration curves than the CC method does (Figure 17).

3.2. Fracture Surfaces

In the second step, the fracture surfaces of the specimens were analyzed to highlight the path of the crack and the presence of different physical phenomena. Note that the crack never seemed to propagate in the glue. The break was either adhesive, between the wood and the glue, or cohesive in the wood, but no cohesive break in the glue was observed when the fracture surfaces were observed under a microscope. This phenomenon has already been reported in wood assemblies, where the glue joint is known to be stronger than wood [55]. To relate the crack propagation and the G_{Ic} values obtained, other phenomena have been identified to classify crack propagation:

For $0^\circ/0^\circ$ specimens:

- Crack at the $0^\circ/0^\circ$ interface. It would seem that this crack is cohesive in the wood close to the glue interface between the two plies at 0° , and sometimes adhesive between the wood and the glue. However, these two rupture modes could be observed in the width of the specimen, so they will be considered together for the $0^\circ/0^\circ$ interface crack propagation (zone **2** in Figure 24)
- Crack migration out of a plane (zone **3** in Figure 24)

For $0^\circ/90^\circ$ specimens:

- Crack at the $0^\circ/90^\circ$ interface (zone **4** in Figure 23)
- Propagation in the 90° ply (Figure 22 and zone **2** in Figure 23)
- Crack migration out of a plane or mixed event (zones 3 and 5 in Figure 23, and 3 in Figure 24)

As the propagation of the crack in the 90° ply seems to be in the lower part of the ply, the hypothesis that can be advanced for this phenomenon is that the upper part (which includes lathe checks) would not allow a simple propagation of the crack because the lathe check would be filled with glue. The crack would then naturally propagate in the lower part of the ply, which offers the least resistance.

In section **3.1**, an average R-curve was plotted for all the specimens. The idea now is to distinguish the different propagation phenomena on each specimen. For example, with specimen $0^\circ/90^\circ$ no. 4, G_{Ic} values are computed from line **1** in Figure 23, according to ASTM D5528 (ASTM 2010). The crack then propagates in the 90° ply (zone **2** in Figure 23) and passes to the interface by tearing fibers (zone **3** in Figure 23). This zone (**3**) is not used for the calculation of the G_{Ic} because it corresponds to a mixed phenomenon (bridging of fibers and passage of the crack at the $0^\circ/90^\circ$ interface). To obtain an average value of G_{Ic} per type of crack propagation according to the classification proposed above, mixed phenomena are not considered since, in mixed zones, the effects of the individual phenomena on the G_{Ic} cannot be distinguished. The crack then propagates to the interface between the 0° and 90° plies (zone **4** in Figure 23). The last part, in purple, corresponds to a similar propagation to zone 3, which cannot be classified and therefore is not considered (zone **5** in Figure 23). The end of the specimen is no longer in the field of view of the cameras and crack tracking is no longer possible (after zone **5** in Figure 23).

A similar analysis was carried out on the $0^\circ/0^\circ$ specimens, as illustrated by the example of specimen no. 1 in Figure 24. The difference here is that only the propagation at the $0^\circ/0^\circ$ interface (zone **2** in Figure 24) and particular events (mainly out-of-plane crack migration for these specimens) were considered (zone **3** in Figure 24).

By performing this analysis on each specimen, it is possible to calculate the crack propagation energy for each previously distinguished area. For the $0^\circ/0^\circ$ specimens, the value calculated is identical to the

mean value obtained in §3.1 (the abnormal values have already been removed from this study as explained in §3.1), $G_{Ic-0^\circ/0^\circ} = 422 \text{ J/m}^2$ (RSD: 30%). For $90^\circ/0^\circ$ specimens, the study of the fracture surfaces reveals different R-curves and different average values depending on the zone of propagation of the crack. To understand the different physical phenomena involved, it is interesting to compare the present results with a theoretical model based on the Euler-Bernoulli beam theory [56]. This model provides the following relations (Equation 5 and Equation 6):

$$C = \frac{2a^3}{3E_I I}$$

Equation 5

$$P(\delta) = \sqrt{\frac{2b^2}{3\delta}} \sqrt{\frac{G_{Ic}^3 E_I (h/2)^3}{12}} = \frac{1}{\sqrt{\delta}} \left(\frac{4}{9} E_I I \right)^{\frac{1}{4}} (b G_{Ic})^{\frac{3}{4}}$$

Equation 6

with I referring to the moment of inertia of a DCB specimen arm and E_I the longitudinal Young's modulus.

By plotting $P=f(\delta)$ using the measured δ displacement, it is possible to visualize experimental and theoretical curves on the same graph. Specimen $0^\circ/90^\circ$ no. 4 is taken as an example here. A comparison of the theoretical values observed with the R-curve of the same specimen gives the minimum and maximum values observed (~ 55 and $\sim 448 \text{ J/m}^2$ in this case).

The differences between the theoretical and experimental curves can be explained. Initially, the experimental curve follows the theoretical curve for $G_{Ic} = 188 \text{ J/m}^2$ (before zone 1 in Figure 25). There is then a quasi-constant force on the $P-\delta$ curve, which means that the energy required for the propagation of the crack increases (zone 1 in Figure 25): when the crack propagates in the 90° ply, it tends to follow lines of least resistance and create some fiber bridging (zone 2 in Figure 25). Fiber bridging is not as frequent in the $0^\circ/90^\circ$ specimens as in the $0^\circ/0^\circ$ specimen but it nevertheless exists and is shown in Figure 26. It should be noted, however, the out-of-plane bridging in the $0^\circ/90^\circ$ specimens seems less marked, given the calculated energies compared to the $0^\circ/0^\circ$ specimens. The subsequent drop in force occurs when the crack migrates in an unstable way at the $0^\circ/90^\circ$ interface

after tearing fibers (zone 3 in Figure 25). It is then easier for the crack to propagate at the interface than between the wood cells and the locally accumulated energy dissipates, hence the fall of G_{Ic} . Note that this propagation at the interface takes place over a very short time; the value of G_{Ic} obtained can be influenced by viscosity phenomena due to wood or glue due to the dynamic propagation. The crack then resumes a tortuous path between the wood cells in the 90° ply, which again explains the increase in the value of G_{Ic} , as was the case in zone 2 in Figure 25 (zone 4 in Figure 25).

Note that, in the case where the crack propagates at the interface, the measurement points taken during the crack propagation are not considered for the calculation of the average value of G_{Ic} , because it is a dynamic propagation. Only the final and stable point is considered when the crack has stabilized. Due to the unstable propagation of the crack, these values underestimate the G_{Ic} (static value) of the interface. Note that the propagation in the $0^\circ/90^\circ$ interface is observed on only two specimens and only a part of the crack propagation occurs at the interface, in both cases, it is an unstable propagation. Once the fracture propagation phenomenon has been detailed, it is possible to plot the R-curves for crack propagation at the $0^\circ/90^\circ$ interface and in the 90° ply (Figure 27).

When the crack propagates in the 90° ply, it moves around the fibers, which contributes to the tortuous appearance of each R-curve. The value obtained for the fracture toughness in the 90° ply is $G_{Ic-90^\circ\text{-ply}} = 247 \text{ J/m}^2$ (RSD: 24%).

When the crack moves towards the $0^\circ/90^\circ$ interface, there is a significant decrease in the value of G_{Ic} . This is because the crack no longer needs to bypass or break fibers to propagate and so requires a smaller amount of energy. The average value of the critical energy is obtained by taking the values calculated once the crack is installed in the interface. In the present case, only two values were obtained; they are visible in Figure 27. The value found for the critical fracture toughness at the interface $0^\circ/90^\circ$ is $G_{Ic-0^\circ/90^\circ\text{-interface}} = 62 \text{ J/m}^2$ (RSD: 28%). However, a low degree of confidence is to apply to this value given the very low number of test configurations on which this phenomenon appeared and its dynamic aspect. The value to use is therefore $G_{Ic-90^\circ\text{-ply}} = 247 \text{ J/m}^2$ (RSD: 24%).

4. Discussion

In the literature, the values of G_{Ic} on a $0^\circ/0^\circ$ interface of LVL or glulam are between about 20 and 850 J/m². These values are summarized in Table 1.

Authors	Material	G_{Ic} (J/m ²) Min/max
[30]	6-ply beech plywood [0°/90°/0°]/[0°/90°/0°]	~20
[28]	9-ply ceiba plywood [undisclosed stacking sequence]	~140 to 200
[33]	Beech glulam	~30 to 80
[37]	Poplar glulam	~120 to 230
[31]	Scots pine glulam	~150 to 250
[32]	Poplar glulam	~200 to 300
[34]	Maritime pine glulam	~220 to 465
[35]	Maritime pine glulam	~ 400 to 550
[36]	Beech glulam	~ 827 ± 239

Table 1 – Comparison of the orders of magnitude of G_{Ic}

Few authors have investigated plywood toughness, which is why some G_{Ic} values obtained on glulam are compared here. It is important to note that the thicknesses of wood lumber and veneers are not identical and therefore there is a scale effect between these materials. However, the differences between the authors' findings can be explained mainly by the type of wood and glue used in the manufacturing of the plywood or glulam characterized. The toughness of a glued assembly is strongly correlated with the nature of the wood-glue combination. In addition, the fracture energy of the assembly will also be influenced by the roughness of the wood, the thickness of the glue joint or Young's modulus of the material characterized [57]. Similarly, a strong dispersion is expected on tests such as DCB applied to wood and wood composite materials due to the heterogeneity of wood material and the variability of its mechanical properties [57]. Some average values for standard composites in aeronautics are summarized in Table 2. The mean value of toughness obtains for $0^\circ/0^\circ$ specimens is in the same order of magnitude as thermoset composites.

Authors	Material	G_{Ic} (J/m ²)
[58]	UD carbon/epoxy 1st generation (type 3506)	60
[39]	UD carbon/epoxy 2nd generation (type M21)	450
[59]	UD carbon/PEEK (type APC-2)	2200
[60]	UD carbon/PPS	1100
[38]	U.D. Glass/epoxy	800
[61]	U.D. Glass-E/polyester	300

Table 2 – Some G_{Ic} values for standard composites in aeronautics [62]

The literature does not provide a value of G_{Ic} for a $0^\circ/90^\circ$ interface in the case of plywood. However, given the results obtained during this study, it can be seen that the value of G_{Ic} for a $0^\circ/90^\circ$ interface ($G_{Ic-90^\circ} = 247 \text{ J/m}^2$ (RSD: 21%)) is lower than for a $0^\circ/0^\circ$ interface ($G_{Ic-0^\circ/0^\circ} = 422 \text{ J/m}^2$ (RSD: 30%)) because fiber bridging is less present than in a $0^\circ/0^\circ$ interface. Note that the value of G_{Ic} for an $0^\circ/0^\circ$ interface measured experimentally overestimates the value of delamination compared to a pure interface without the effects of fiber bridging and fiber rupture. It is therefore possible to wonder whether the toughness characterized for a $0^\circ/90^\circ$ interface is not to be preferred if the aim is to obtain a numerical value of the mode I fracture toughness of a plywood interface by limiting the influence of fiber bridging. Moreover, according to research [63], the interface $0^\circ/90^\circ$ is the most susceptible to delamination in cases of impact-induced delamination. The value obtained will be a value that is less influenced by fiber bridging and closer to the theoretical value that will subsequently be used for the implementation of a finite element model to simulate the glued interface.

It is also interesting to compare the fracture pattern found in this study with those recorded in DCB tests on carbon fiber composite materials. The configuration with a $0^\circ/0^\circ$ interface allows the boundary value of G_{Ic} to be lowered in the case of synthetic composite materials because it is the configuration that gives the least fiber bridging and the 0° fibers at the interface prevent delamination migration [39], [64], [65]. Figure 28 illustrates a representative side view of the crack path of such an interface.

In the case of wood, the crack rapidly migrates outside the initial interface. There are several possible explanations for this phenomenon. First, the wood has fibers with a non-zero out-of-plane deviation of the fiber angle due to the manufacturing process, a situation that is much less common for composites. Additionally, the thickness of a wood veneer can be composed of earlywood and latewood (Figure 5) and this heterogeneity could create an easier propagation path for the crack. Finally, in wood assemblies, the glue joint is known to be stronger than wood [55]. This phenomenon can cause the crack to propagate cohesively near the interface for the $0^\circ/0^\circ$ specimens and mostly in the 90° ply for the $0^\circ/90^\circ$ specimens. This is exactly what has been observed on IMA/M21E composites: the glued interface is stronger than the plies [23], [66].

In the second configuration of composite materials, with a $0^\circ/90^\circ$ interface, the crack may change plane during delamination [39] (Figure 29). This delamination migration in synthetic composite material tends to increase the fracture area and to dissipate more energy [40]. According to Sebaey et al., their numerical model demonstrates that as the bending stiffness of specimen arms decreases, there is an increased propensity for delamination migration at the interface [67]. However, for plywood, delamination migration doesn't occur on specimen with $0^\circ/90^\circ$ interface.

Concerning fiber bridging, the phenomenon is less important for this configuration compared to specimens with $0^\circ/0^\circ$ interface. Due to the propagation of the crack in the 90° ply, the few fiber bridging behavior observed is comparable to that of a $90^\circ/90^\circ$ interface in synthetic composite [40], [65].

Considering the nature of the wood, with the presence of out-of-plane fibers and a greater fiber bridging, it is possible to explain why the value of G_{Ic} for a $0^\circ/0^\circ$ interface is not a lower bound G_{Ic} value for plywood while this is the case for composite materials [39], [40], [50]. In addition, fracture pattern and crack propagation appear similar when crack propagations are compared for $0^\circ/90^\circ$ interfaces in the cases of plywood and composite materials.

5. Conclusions and Perspectives

The effects of interfacial orientation for two different configurations were investigated in DCB tests on poplar plywood. The following conclusions can be drawn from the results of the study:

- On the R-curves, $G_{Ic-0^\circ/0^\circ}$ tends to increase, due to fiber bridging, while the average value of $G_{Ic-0^\circ/90^\circ}$ remains quasi-constant, slightly decreasing, as a function of the crack propagation.
- The values of $G_{Ic-0^\circ/0^\circ}$ ($G_{Ic-0^\circ/0^\circ} = 422 \text{ J/m}^2$ (RSD: 30%)) are more scattered than $G_{Ic-0^\circ/90^\circ}$ ($G_{Ic-0^\circ/90^\circ} = 247 \text{ J/m}^2$ (RSD: 21%)). This is explained by the presence of fiber bridging during the crack propagation in the case of the $0^\circ/0^\circ$ interface.
- On average, the $G_{Ic-0^\circ/0^\circ}$ has a higher value than $G_{Ic-0^\circ/90^\circ}$, due to the presence of fiber bridging. It is interesting to perform DCB tests with a $0^\circ/90^\circ$ interface to obtain G_{Ic} values for plywood, for the development of numerical models. This interface corresponds to those most likely to delaminate. The apparent toughness, i.e. the toughness computed with the influence of structural effects such as fiber bridging, could differ from the intrinsic material toughness value. However, the values presented in this article provide values for comparing the effect of the interface on delamination. It should also be noted that some fiber bridging also influences the values obtained on $0^\circ/90^\circ$ specimens.

To implement a numerical model of wood-based composite, specimen characterization with $0^\circ/90^\circ$ interfaces seems to provide a lower bound for the interface toughness value that could serve as a reference for modelling glued interfaces of plywood or LVL, for example. However, further research is needed to determine the influence of new interface orientations on these toughness values and to identify the influence of this interface on the measured values. In addition, in low-velocity impact failure, mode I initiate the delamination in composite laminates, but then mode II (plane shear) is predominant in the propagation of the crack due to high shear stress at the interface [68]. To set up a digital model of plywood, it would then be necessary to characterize mode II toughness through, for example, ENF (End Notched Flexure) tests. However, it has to be underlined that delamination migration can also occur in mode II propagation, it's already observed in LVL [69] and in carbon fibre composite with ENF tests [70], [71].

6. Acknowledgments

The research that led to the results presented above received funds from the French National Research Agency under the BOOST project (ANR-21-CE43-0008-01). The authors thank the LaBoMaP Laboratory, Cluny, France for providing the Poplar veneers used in this study, through the research project ANR BOOST.

7. References

- [1] G. Wimmers, 'Wood: a construction material for tall buildings', *Nat. Rev. Mater.*, vol. 2, p. 17051, Jul. 2017, doi: 10.1038/natrevmats.2017.51.
- [2] J. Ye and C. Fivet, 'The zaojing: review of a unique wooden construction typology', *Int. J. Constr. Hist. Soc.*, vol. 35, no. 1, pp. 22–49, Jun. 2020, doi: 10.5281/zenodo.3941502.
- [3] B. Castanie, C. Bouvet, and M. Ginot, 'Review of composite sandwich structure in aeronautic applications', *Compos. Part C Open Access*, vol. 1, p. 100004, Aug. 2020, doi: 10.1016/j.jcomc.2020.100004.
- [4] G. Jungmeier, F. Werner, A. Jarnehammar, C. Hohenthal, and K. Richter, 'Allocation in LCA of wood-based products experiences of cost action E9: Part I. Methodology', *Int. J. Life Cycle Assess.*, vol. 7, no. 5, pp. 290–294, Sep. 2002, doi: 10.1007/BF02978890.
- [5] G. Jungmeier, F. Werner, A. Jarnehammar, C. Hohenthal, and K. Richter, 'Allocation in LCA of wood-based products experiences of cost action E9: Part II. Examples', *Int. J. Life Cycle Assess.*, vol. 7, no. 6, pp. 369–375, Nov. 2002, doi: 10.1007/BF02978686.
- [6] R. Bergman, M. Puettmann, A. Taylor, and K. E. Skog, 'The Carbon Impacts of Wood Products', *For. Prod. J.*, vol. 64, no. 7–8, pp. 220–231, Dec. 2014, doi: 10.13073/FPJ-D-14-00047.
- [7] C. Cornillier and E. Vial, 'L'Analyse de Cycle de Vie (ACV) appliquée aux produits bois : bilan énergétique et prise en compte du carbone biomasse', presented at the IXème Colloque Sciences et Industrie du Bois, 2008, p. 16.
- [8] K. Tamanna, S. N. Raman, M. Jamil, and R. Hamid, 'Utilization of wood waste ash in construction technology: A review', *Constr. Build. Mater.*, vol. 237, p. 117654, Mar. 2020, doi: 10.1016/j.conbuildmat.2019.117654.
- [9] Finnish Woodworking Industries Federation, Ed., *LVL handbook Europe*. Helsinki: Federation of the Finnish Woodworking Industries, 2019.
- [10] Y. Kiliç, E. Burdurlu, G. C. Elibol, and M. Ulupinar, 'Effect of Layer Arrangement on Expansion, Bending Strength and Modulus of Elasticity of Solid Wood and Laminated Veneer Lumber (LVL) Produced from Pine and Poplar', p. 7, 2010.
- [11] R. H. Leicester and R. C. Bunker, 'Fracture at butt joints in laminated pine', *For. Prod J* 192 59-60, 1969.
- [12] H. Sasaki and A. A. Abdullahi, 'Lumber: Laminated Veneer', in *Reference Module in Materials Science and Materials Engineering*, Elsevier, 2016, p. B9780128035818020000. doi: 10.1016/B978-0-12-803581-8.01989-5.
- [13] J. A. Youngquist, T. L. Laufenberg, and B. S. Bryant, 'End jointing of laminated veneer lumber for structural use', *For. Prod. J.*, p. 8, 1984.
- [14] R. Guélou, F. Eyma, A. Cantarel, S. Rivallant, and B. Castanié, 'A comparison of three wood species (poplar, birch and oak) for crash application', *Eur. J. Wood Wood Prod.*, Aug. 2022, doi: 10.1007/s00107-022-01871-x.
- [15] J. Susainathan, F. Eyma, E. De Luycker, A. Cantarel, C. Bouvet, and B. Castanie, 'Experimental investigation of compression and compression after impact of wood-based sandwich structures', *Compos. Struct.*, vol. 220, pp. 236–249, Jul. 2019, doi: 10.1016/j.compstruct.2019.03.095.
- [16] R. Guélou, F. Eyma, A. Cantarel, S. Rivallant, and B. Castanié, 'Static crushing of wood based sandwich composite tubes', *Compos. Struct.*, vol. 273, 2021, doi: 10.1016/j.compstruct.2021.114317.

- [17] R. Guélou, F. Eyma, A. Cantarel, S. Rivallant, and B. Castanié, 'Crashworthiness of poplar wood veneer tubes', *Int. J. Impact Eng.*, vol. 147, p. 103738, Jan. 2021, doi: 10.1016/j.ijimpeng.2020.103738.
- [18] R. Guélou, F. Eyma, A. Cantarel, S. Rivallant, and B. Castanié, 'Dynamic crushing of wood-based sandwich composite tubes', *Mech. Adv. Mater. Struct.*, pp. 1–21, Oct. 2021, doi: 10.1080/15376494.2021.1991533.
- [19] J. Susainathan, F. Eyma, E. De Luycker, A. Cantarel, and B. Castanie, 'Manufacturing and quasi-static bending behavior of wood-based sandwich structures', *Compos. Struct.*, vol. 182, pp. 487–504, Dec. 2017, doi: 10.1016/j.compstruct.2017.09.034.
- [20] J. Susainathan, F. Eyma, E. De Luycker, A. Cantarel, and B. Castanie, 'Experimental investigation of impact behavior of wood-based sandwich structures', *Compos. Part Appl. Sci. Manuf.*, vol. 109, pp. 10–19, Jun. 2018, doi: 10.1016/j.compositesa.2018.02.029.
- [21] J. Susainathan, F. Eyma, E. De Luycker, A. Cantarel, and B. Castanie, 'Numerical modeling of impact on wood-based sandwich structures', *Mech. Adv. Mater. Struct.*, vol. 27, no. 18, Art. no. 18, Sep. 2020, doi: 10.1080/15376494.2018.1519619.
- [22] S. Abrate, B. Castanié, and Y. D. S. Rajapakse, Eds., *Dynamic Failure of Composite and Sandwich Structures*, vol. 192. in Solid Mechanics and Its Applications, vol. 192. Dordrecht: Springer Netherlands, 2013. doi: 10.1007/978-94-007-5329-7.
- [23] L. Adam, C. Bouvet, B. Castanié, A. Daidié, and E. Bonhomme, 'Discrete ply model of circular pull-through test of fasteners in laminates', *Compos. Struct.*, vol. 94, no. 10, pp. 3082–3091, Oct. 2012, doi: 10.1016/j.compstruct.2012.05.008.
- [24] C. Bouvet, B. Castanié, M. Bizeul, and J.-J. Barrau, 'Low velocity impact modelling in laminate composite panels with discrete interface elements', *Int. J. Solids Struct.*, vol. 46, no. 14, pp. 2809–2821, Jul. 2009, doi: 10.1016/j.ijsolstr.2009.03.010.
- [25] J. Serra, C. Bouvet, B. Castanié, and C. Petiot, 'Scaling effect in notched composites: The Discrete Ply Model approach', *Compos. Struct.*, vol. 148, pp. 127–143, Jul. 2016, doi: 10.1016/j.compstruct.2016.03.062.
- [26] J. Konnerth, W. Gindl, M. Harm, and U. Müller, 'Comparing dry bond strength of spruce and beech wood glued with different adhesives by means of scarf- and lap joint testing method', *Holz Als Roh- Werkst.*, vol. 64, no. 4, pp. 269–271, Aug. 2006, doi: 10.1007/s00107-006-0104-1.
- [27] F. Lachaud, 'Delaminage de matériaux composites à fibres de carbone et à matrices organiques : étude numérique et expérimentale, suivi par émission acoustique', PhD Thesis, Université de Toulouse - ISAE, Toulouse, 1997.
- [28] A. El Moustaphaoui, A. Chouaf, and K. Kimakh, 'Experimental and numerical study of the delamination of Ceiba plywood under mode I, mode II and mixed-mode (I + II) loading using the DCB, ELS and MMF tests', *Int. J. Fract.*, Jun. 2021, doi: 10.1007/s10704-021-00557-4.
- [29] A. El Moustaphaoui, A. Chouaf, K. Kimakh, and M. Chergui, 'Characterization of ceiba plywood delamination in mode I using an energetic criterion', *Wood Res.*, vol. 64, p. 12, 2019.
- [30] M. N. Baba, F. Dogaru, I. Curtu, G. Dinu, and M. Bayer, 'Experimental Determination of Interlaminar Fracture Toughness of Wood Laminated Composite Specimens under DCB Test', *Mater. Plast.*, p. 5, 2010.
- [31] Y. Zhao, Z. Li, and B. Xu, 'Mixed-mode (I/II) interlaminar fracture of glued-laminated timber', *Mater. Des.*, vol. 131, pp. 210–218, Oct. 2017, doi: 10.1016/j.matdes.2017.05.070.
- [32] J. Jennings, 'Investigating the Surface Energy, and Bond Performance of Compression Densified Wood', Blacksburg, Virginia, 2003.
- [33] M. Rhême, J. Botsis, J. Cugnoni, and P. Navi, 'Influence of the moisture content on the fracture characteristics of welded wood joint. Part 1: Mode I fracture', *Holzforschung*, vol. 67, no. 7, pp. 747–754, 2013.
- [34] J. Xavier, J. Morais, N. Dourado, and M. F. S. F. De Moura, 'Measurement of Mode I and Mode II Fracture Properties of Wood-Bonded Joints', *J. Adhes. Sci. Technol.*, vol. 25, no. 20, pp. 2881–2895, Jan. 2011, doi: 10.1163/016942411X576563.
- [35] F. G. A. Silva, J. Xavier, F. A. M. Pereira, J. J. L. Morais, N. Dourado, and M. F. S. F. Moura, 'Determination of cohesive laws in wood bonded joints under mode I loading using the DCB test', *Holzforschung*, vol. 67, no. 8, Art. no. 8, Dec. 2013, doi: 10.1515/hf-2013-0012.

- [36] S. Myslicki, T. Vallée, O. Bletz-Mühldorfer, F. Diehl, L. C. Lavarec, and R. Créac'Hcadec, 'Fracture mechanics based joint capacity prediction of glued-in rods with beech laminated veneer lumber', *J. Adhes.*, vol. 95, no. 5–7, pp. 405–424, Jun. 2019, doi: 10.1080/00218464.2018.1538879.
- [37] C. R. Scoville, 'Characterizing the Durability of PF and pMDI Adhesive Wood Composites Through Fracture Testing', PhD Thesis, Virginia Tech, 2001. Accessed: May 09, 2022. [Online]. Available: <https://vtechworks.lib.vt.edu/handle/10919/35353>
- [38] D. Gay, *Composite Materials: Design and Applications*, 3rd edition. CRC Press, 2014.
- [39] P. Prombut, 'Caractérisation de la propagation de délaminage des stratifiées composites multidirectionnelles', PhD Thesis, Université de Toulouse III – Paul Sabatier, Toulouse, 2007.
- [40] Y. Gong *et al.*, 'Delamination in carbon fiber epoxy DCB laminates with different stacking sequences: R-curve behavior and bridging traction-separation relation', *Compos. Struct.*, vol. 262, p. 113605, Apr. 2021, doi: 10.1016/j.compstruct.2021.113605.
- [41] G. R. Irwin and J. A. Kies, 'The welding journal', *Res Suppl*, vol. 33, p. 193, 1954.
- [42] L. Denaud *et al.*, 'Influence of Peeling Process Parameters on Veneer Lathe Check Properties', presented at the 24th International Wood Machining Semina, Corvallis, OR, USA, Aug. 2019.
- [43] G. Pot, L. Denaud, J.-C. Butaud, S. Girardon, R. Collet, and F. Cottin, 'Experimental study of the influence of veneer lathe checks on LVL elastic mechanical properties', Aug. 2016.
- [44] S. Stefanowski, R. Frayssinhes, G. Pinkowski, and L. Denaud, 'Study on the in-process measurements of the surface roughness of Douglas fir green veneers with the use of laser profilometer', *Eur. J. Wood Wood Prod.*, vol. 78, no. 3, pp. 555–564, May 2020, doi: 10.1007/s00107-020-01529-6.
- [45] I. Rahayu, L. Denaud, R. Marchal, and W. Darmawan, 'Ten new poplar cultivars provide laminated veneer lumber for structural application', *Ann. For. Sci.*, vol. 72, no. 6, pp. 705–715, Sep. 2015, doi: 10.1007/s13595-014-0422-0.
- [46] J. Gáborík and K. Káčerová, 'Bending properties of laminated wood from juvenile poplar.', *Proc. 2nd Int. Sci. Conf. Woodwork. Tech. Zalesina Croat. 11-15 Sept. 2007*, pp. 233–240, 2007.
- [47] F. F. P. Kollmann, W. A. Côté, E. W. Kuenzi, and A. J. Stamm, *Principles of Wood Science and Technology: Solid wood*. G. Allen & Unwin, 1968.
- [48] W. Leggate, R. McGavin, and H. Bailleres, *A guide to manufacturing rotary veneer and products from small logs*, ACIAR Monograph. 2017.
- [49] P. Reu, 'All about speckles: Speckle Size Measurement', *Exp. Tech.*, vol. 38, no. 6, pp. 1–2, Nov. 2014, doi: 10.1111/ext.12110.
- [50] A. Ramji, Y. Xu, M. Yasaee, M. Grasso, and P. Webb, 'Delamination migration in CFRP laminates under mode I loading', *Compos. Sci. Technol.*, vol. 190, p. 108067, Apr. 2020, doi: 10.1016/j.compscitech.2020.108067.
- [51] T. Lisle, C. Bouvet, N. Hongkarnjanakul, M.-L. Pastor, S. Rivallant, and P. Margueres, 'Measure of fracture toughness of compressive fiber failure in composite structures using infrared thermography', *Compos. Sci. Technol.*, vol. 112, pp. 22–33, May 2015, doi: 10.1016/j.compscitech.2015.03.005.
- [52] M. Pramreiter, S. C. Bodner, J. Keckes, A. Stadlmann, C. Kumpenza, and U. Müller, 'Influence of Fiber Deviation on Strength of Thin Birch (*Betula pendula* Roth.) Veneers', *Materials*, vol. 13, no. 7, Art. no. 7, Mar. 2020, doi: 10.3390/ma13071484.
- [53] J. L. Gómez-Royuela, A. Majano-Majano, A. J. Lara-Bocanegra, J. Xavier, and M. F. S. F. de Moura, 'Evaluation of R-curves and cohesive law in mode I of European beech', *Theor. Appl. Fract. Mech.*, vol. 118, p. 103220, Apr. 2022, doi: 10.1016/j.tafmec.2021.103220.
- [54] S. Hashemi, A. Jame Kinlock, and J. M. Williams, 'The analysis of interlaminar fracture in uniaxial fibre-polymer composites', *Proc. R. Soc. Lond. Math. Phys. Sci.*, vol. 427, no. 1872, pp. 173–199, Jan. 1990, doi: <https://doi.org/10.1098/rspa.1990.0007>.
- [55] R. J. Ross and F. P. Laboratory. USDA Forest Service., 'Wood handbook : wood as an engineering material', U.S. Department of Agriculture, Forest Service, Forest Products Laboratory, Madison, WI, FPL-GTR-190, 2010. doi: 10.2737/FPL-GTR-190.
- [56] N. Ben Salem, 'Fiabilité des assemblages structuraux collés pour applications spatiales', PhD Thesis, Bordeaux 1, 2012. Accessed: Oct. 19, 2022. [Online]. Available: <https://www.theses.fr/2012BOR14681>

- [57] G. Pluvinaige, *La rupture du bois et de ses composites*, Cépaduès-Éditions. 1992. Accessed: Aug. 24, 2021. [Online]. Available: <https://www.eyrolles.com/BTP/Livre/la-rupture-du-bois-et-de-ses-composites-9782854282924/>
- [58] B. W. Kim and A. H. Mayer, 'Influence of fiber direction and mixed-mode ratio on delamination fracture toughness of carbon/epoxy laminates', *Compos. Sci. Technol.*, vol. 63, no. 5, pp. 695–713, Apr. 2003, doi: 10.1016/S0266-3538(02)00258-0.
- [59] S. Hashemi, A. J. Kinloch, and J. G. Williams, 'The Effects of Geometry, Rate and Temperature on the Mode I, Mode II and Mixed-Mode I/II Interlaminar Fracture of Carbon-Fibre/Poly(ether-ether ketone) Composites', *J. Compos. Mater.*, vol. 24, no. 9, pp. 918–956, Sep. 1990, doi: 10.1177/002199839002400902.
- [60] F. Sacchetti, W. J. B. Grouve, L. L. Warnet, and I. F. Villegas, 'Effect of cooling rate on the interlaminar fracture toughness of unidirectional Carbon/PPS laminates', *Eng. Fract. Mech.*, vol. 203, pp. 126–136, Nov. 2018, doi: 10.1016/j.engfracmech.2018.02.022.
- [61] A. Szekrényes, 'Delamination fracture analysis in the GII–GIII plane using prestressed transparent composite beams', *Int. J. Solids Struct.*, vol. 44, no. 10, pp. 3359–3378, May 2007, doi: 10.1016/j.ijsolstr.2006.09.029.
- [62] C. Bouvet, 'Mécanique de la rupture des composites : délaminage et fissuration', *Systèmes Aéronautiques Spatiaux*, Feb. 2019, doi: 10.51257/a-v1-trp4043.
- [63] D. Liu, 'Impact-Induced Delamination: A View of Bending Stiffness Mismatching', *J. Compos. Mater.*, vol. 22, 1988.
- [64] A. Sohrabi, M. Pourhosseinsahi, and B. Mohammadi, 'Prediction of mode I fracture behavior of delaminated 0//90 interface in cross-ply laminated composites from the SERR of classical unidirectional DCB specimen', *Compos. Struct.*, vol. 317, p. 117080, Aug. 2023, doi: 10.1016/j.compstruct.2023.117080.
- [65] M. S. Bin Mohamed Rehan, J. Rousseau, S. Fontaine, and X. J. Gong, 'Experimental study of the influence of ply orientation on DCB mode-I delamination behavior by using multidirectional fully isotropic carbon/epoxy laminates', *Compos. Struct.*, vol. 161, pp. 1–7, Feb. 2017, doi: 10.1016/j.compstruct.2016.11.036.
- [66] S. Chaïbi, 'Prévision des endommagements induits par un impact basse vitesse/basse énergie au sein de matériaux composites stratifiés carbone-epoxy de dernière génération', PhD Thesis, Université de Toulouse - ISAE, Toulouse, 2022.
- [67] T. A. Sebaey, N. Blanco, C. S. Lopes, and J. Costa, 'Numerical investigation to prevent crack jumping in Double Cantilever Beam tests of multidirectional composite laminates', *Compos. Sci. Technol.*, vol. 71, no. 13, pp. 1587–1592, Sep. 2011, doi: 10.1016/j.compscitech.2011.07.002.
- [68] C. Bouvet, S. Rivallant, and J. J. Barrau, 'Low velocity impact modeling in composite laminates capturing permanent indentation', *Compos. Sci. Technol.*, vol. 72, no. 16, pp. 1977–1988, Nov. 2012, doi: 10.1016/j.compscitech.2012.08.019.
- [69] B. Franke and P. Quenneville, 'Analysis of the fracture behavior of Radiata Pine timber and Laminated Veneer Lumber', *Eng. Fract. Mech.*, vol. 116, pp. 1–12, Jan. 2014, doi: 10.1016/j.engfracmech.2013.12.004.
- [70] S. Oshima, A. Mamishin, M. Hojo, M. Nishikawa, N. Matsuda, and M. Kanesaki, 'High-resolution in situ characterization of micromechanisms in CFRP laminates under mode II loading', *Eng. Fract. Mech.*, vol. 260, p. 108189, Feb. 2022, doi: 10.1016/j.engfracmech.2021.108189.
- [71] M. Olave, I. Vara, H. Usabiaga, L. Aretxabaleta, S. V. Lomov, and D. Vandepitte, 'Nesting effect on the mode II fracture toughness of woven laminates', *Compos. Part Appl. Sci. Manuf.*, vol. 74, pp. 174–181, Jul. 2015, doi: 10.1016/j.compositesa.2015.03.020.
- [72] N. M. M. Dourado, M. F. S. F. de Moura, J. J. L. Morais, and M. A. L. Silva, 'Estimate of resistance-curve in wood through the double cantilever beam test', *Holzforschung*, vol. 64, no. 1, Jan. 2010, doi: 10.1515/hf.2010.010.
- [73] R. Duriet *et al.*, 'New Perspectives for LVL Manufacturing from Wood of Heterogeneous Quality—Part. 1: Veneer Mechanical Grading Based on Online Local Wood Fiber Orientation Measurement', *Forests*, vol. 12, no. 9, Art. no. 9, Sep. 2021, doi: 10.3390/f12091264.
- [74] H. G. Richter, K. Gembruch, and G. Koch, 'CITESwoodID - introduction', *delta-intkey*, Sep. 20, 2019. <https://www.delta-intkey.com/citeswood/en/intro.htm> (accessed Jan. 13, 2023).

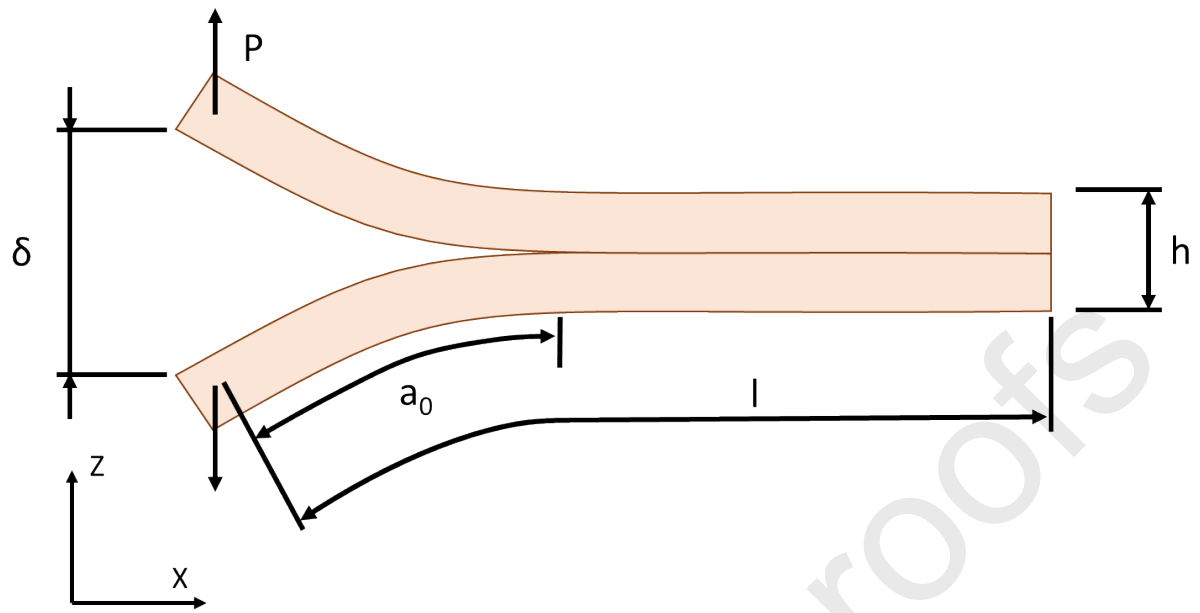


Figure 1- Sketch of the double cantilever beam [72]

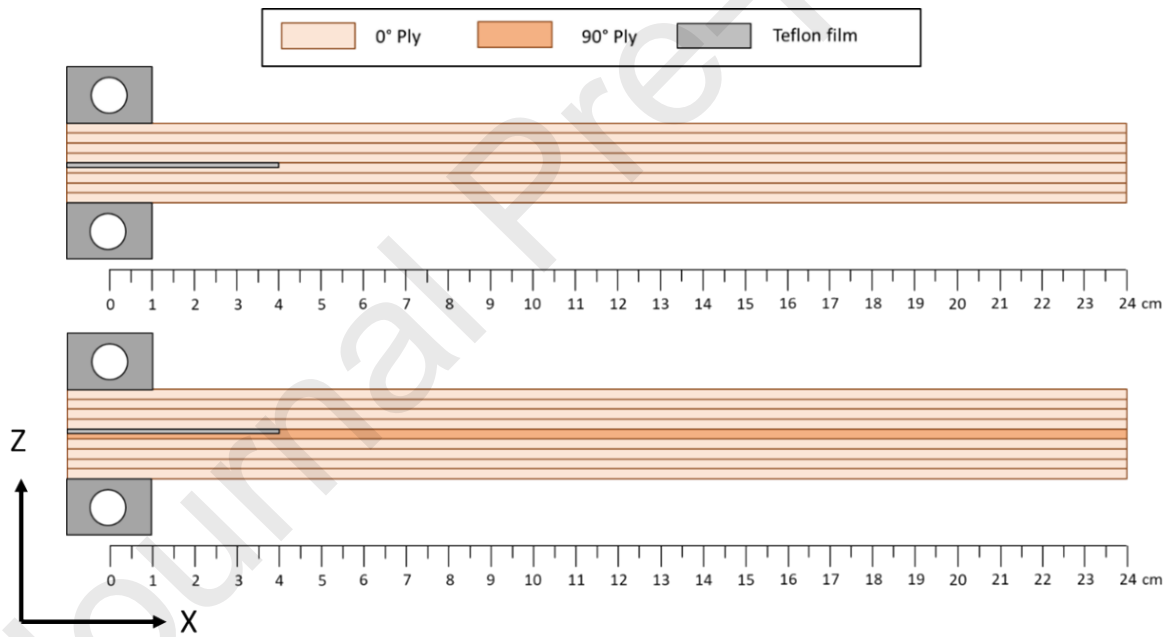


Figure 2- DCB specimen configuration for 0°/0° interface (top) and 0°/90° interface (bottom)

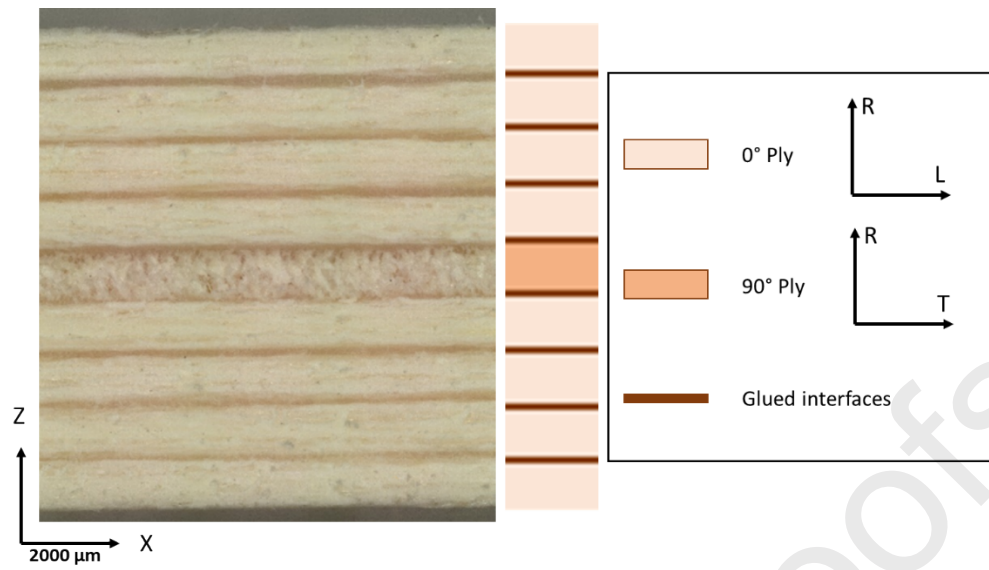


Figure 3- Microscope visualization of 0°/90° specimen thickness

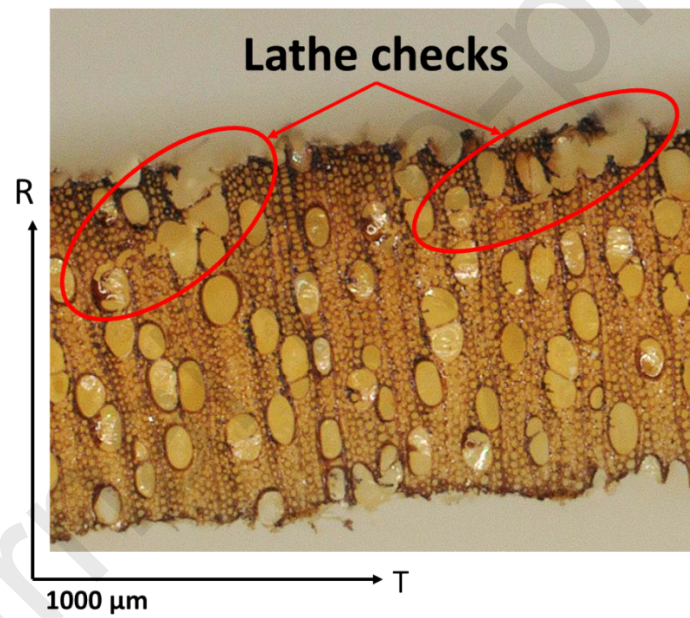


Figure 4- Visible lathe checks on the poplar ply

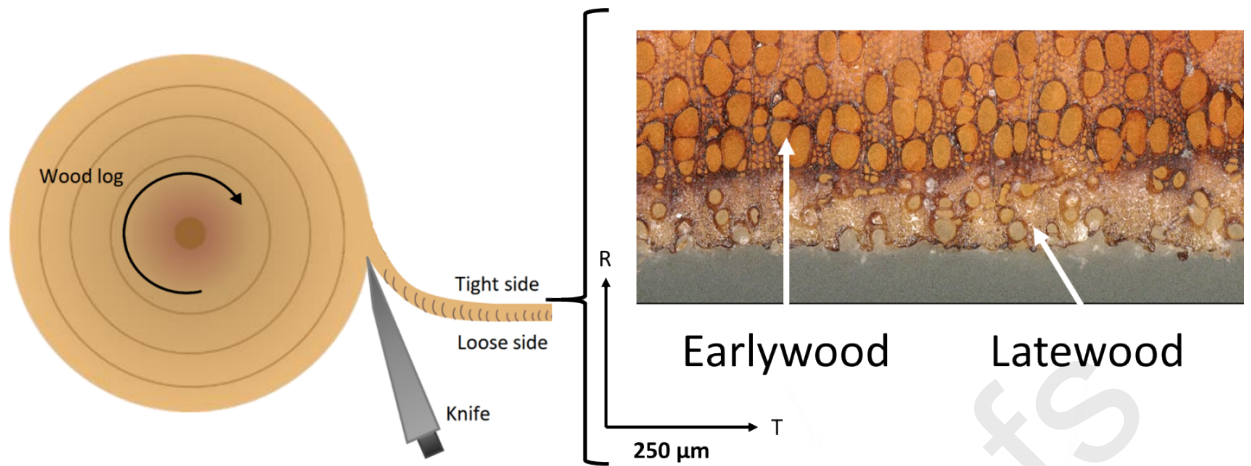


Figure 5 – Illustration of the veneer production process (left) [73] and a microscopic view of earlywood and latewood on veneers (right)

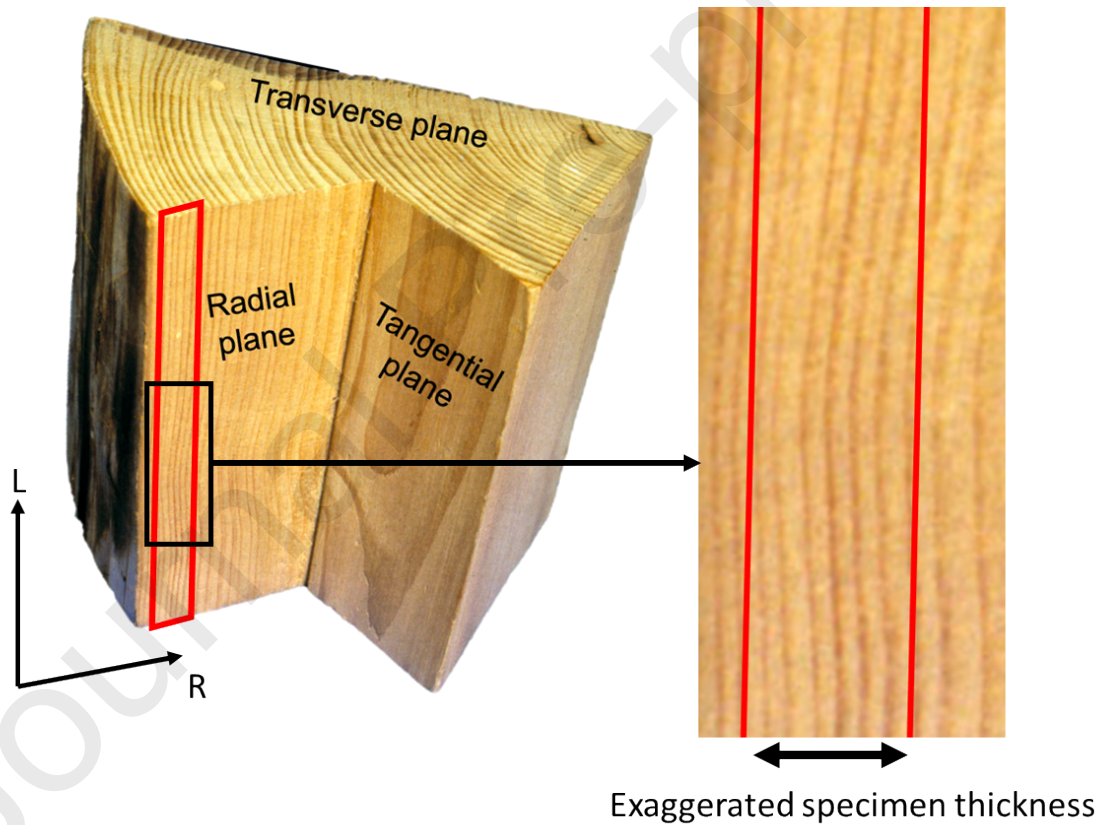


Figure 6 – An exaggerated representation of veneer LR plane on a wood log [74]

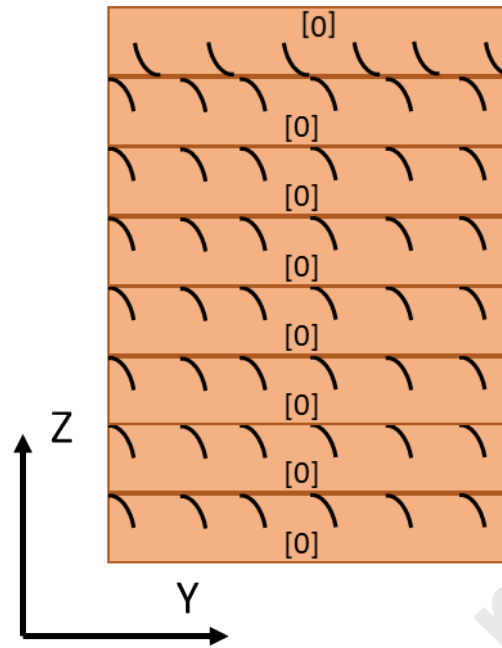


Figure 7- Stacking of the veneer of DCB 0°/0° specimens

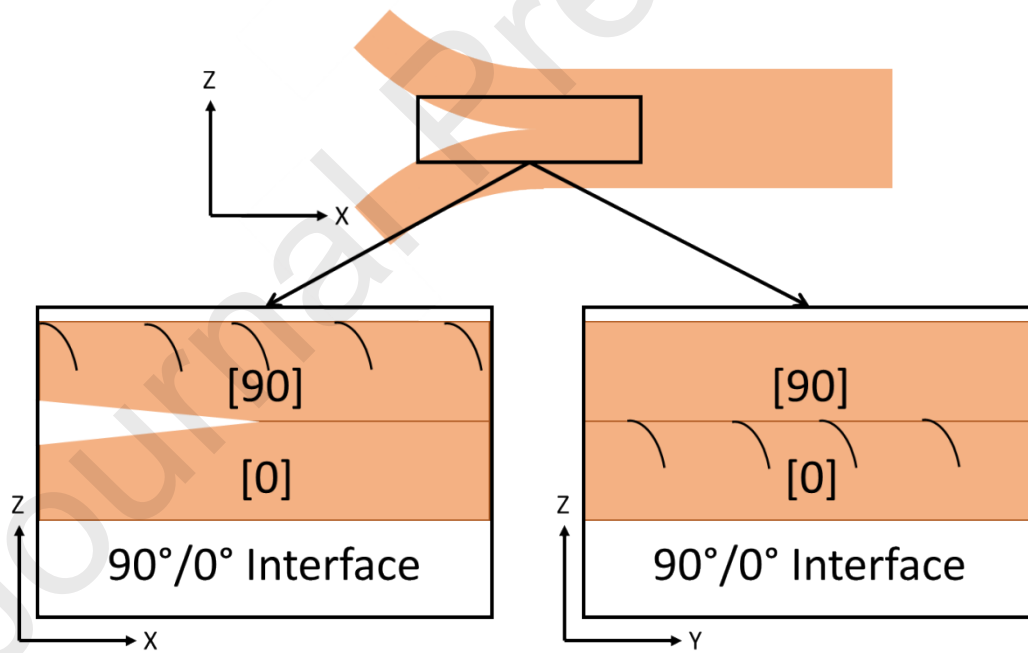


Figure 8- Stacking of the veneer at the interface of DCB 0°/90° specimens

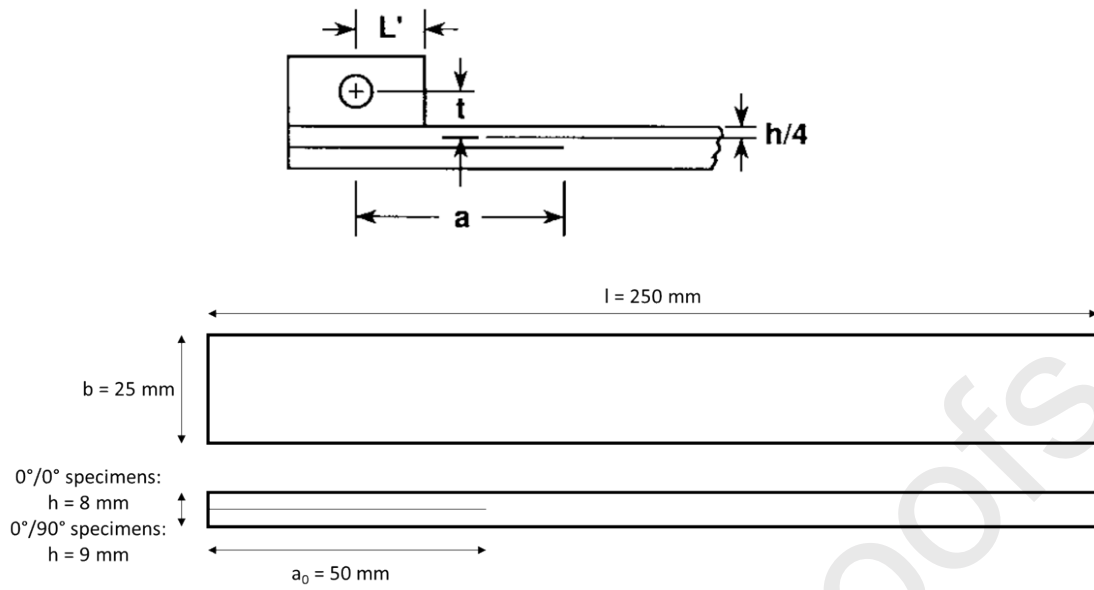


Figure 9- DCB specimen shape used in the experiments

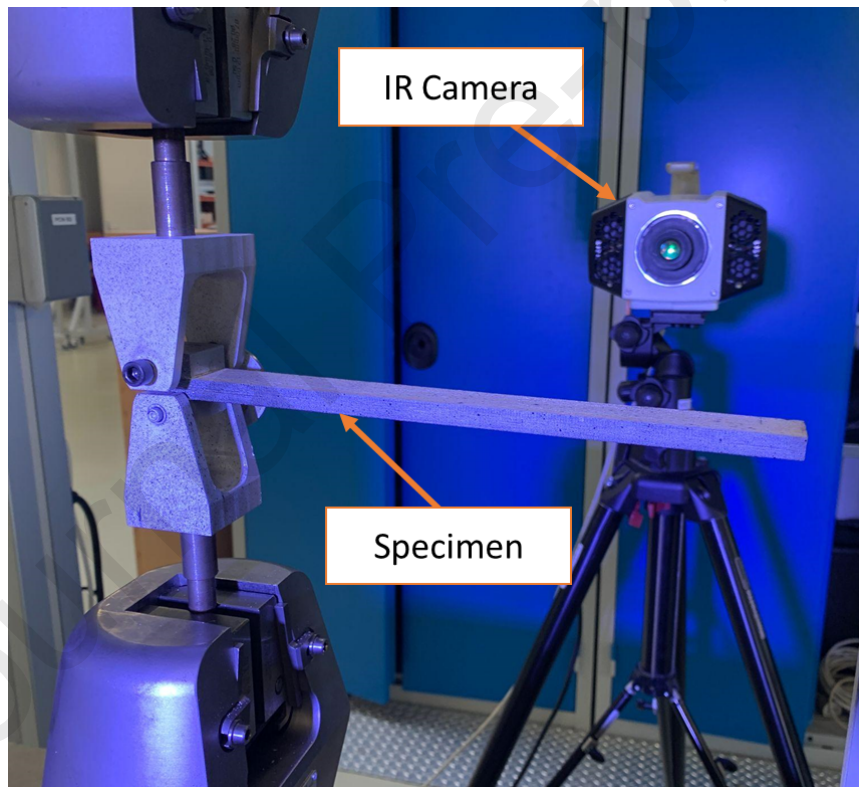


Figure 10- Experimental Setup used during the DCB test

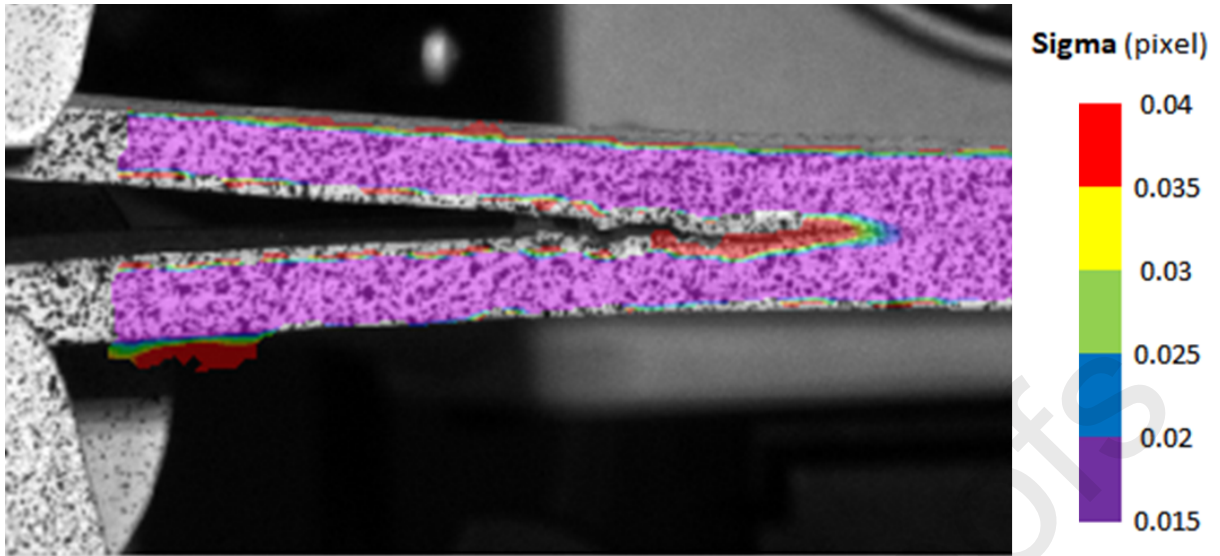


Figure 11 – Sigma visualization for one 0°/90° specimen (*Colored figure*)

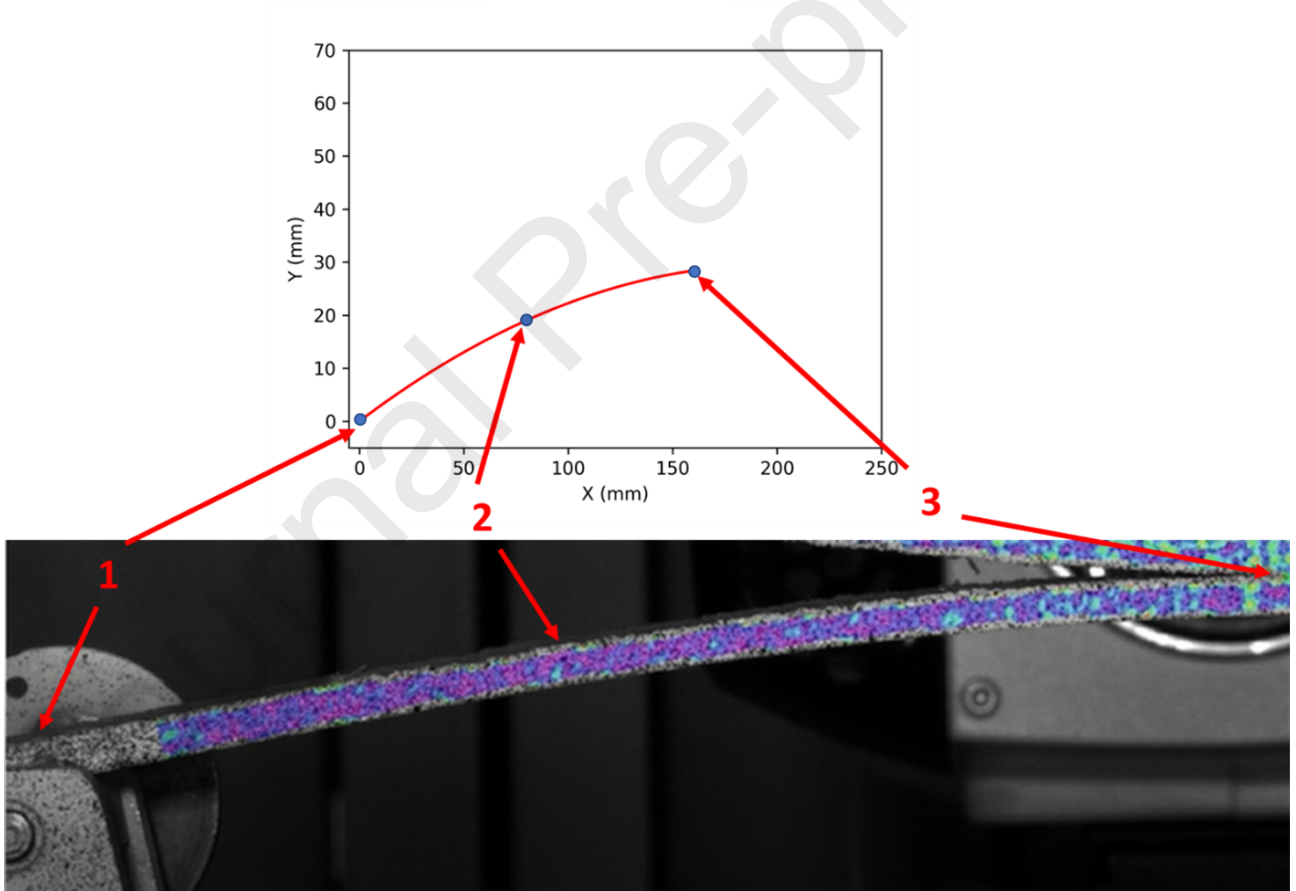


Figure 12 – Three-point interpolation used to obtain the crack length (*Colored figure*)

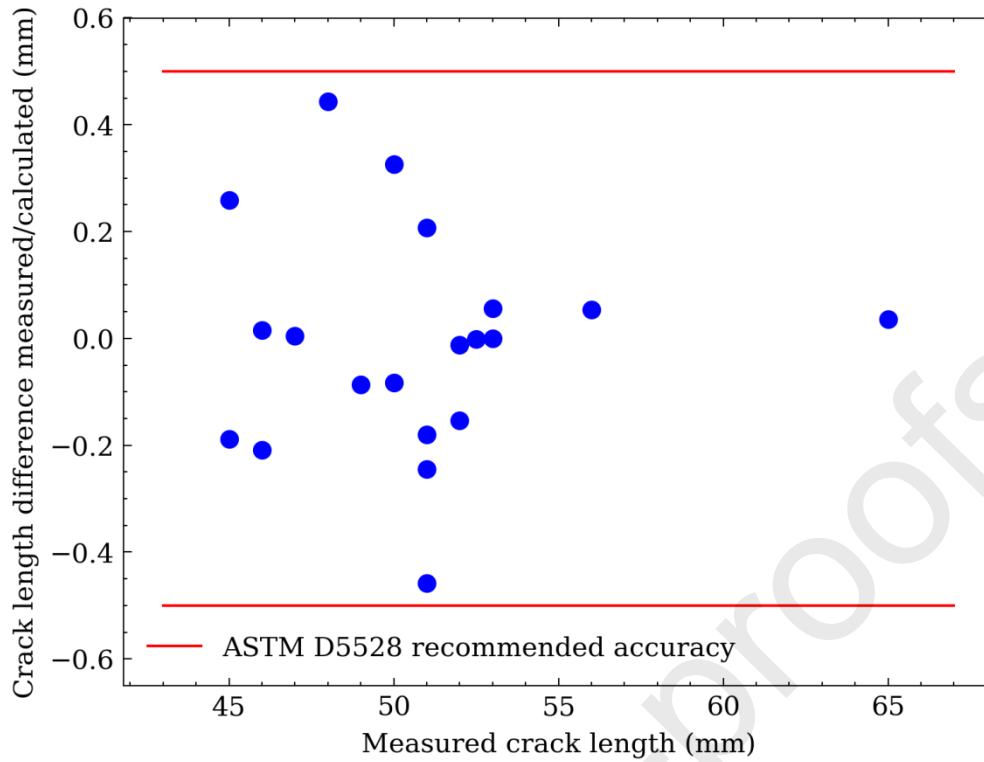


Figure 13 – Difference between measured and calculated initial crack length



Figure 14 – Illustration of the crack path leaving the interfacial $0^\circ/0^\circ$ due to fiber out-of-plane angle

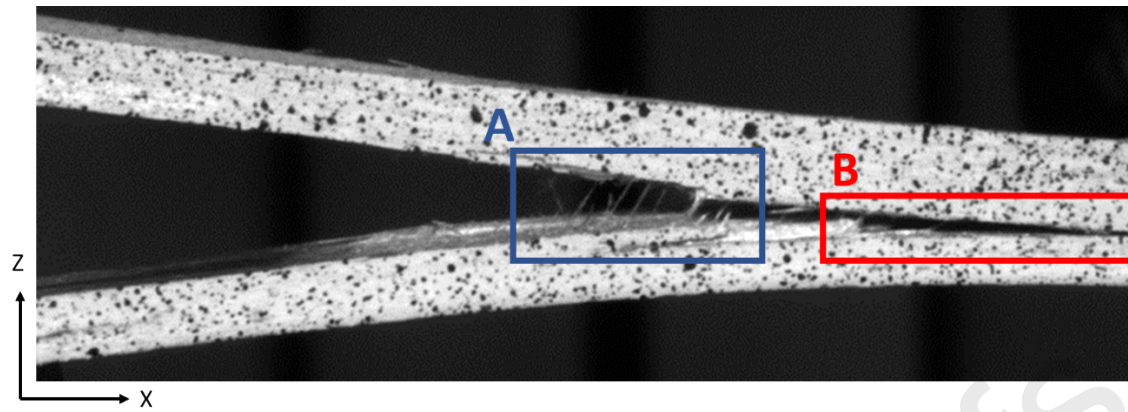


Figure 15 – Post-mortem of specimen $0^\circ/0^\circ$ no. 4 with fiber bridging (A) and crack that has migrated out of the initial interface (B)

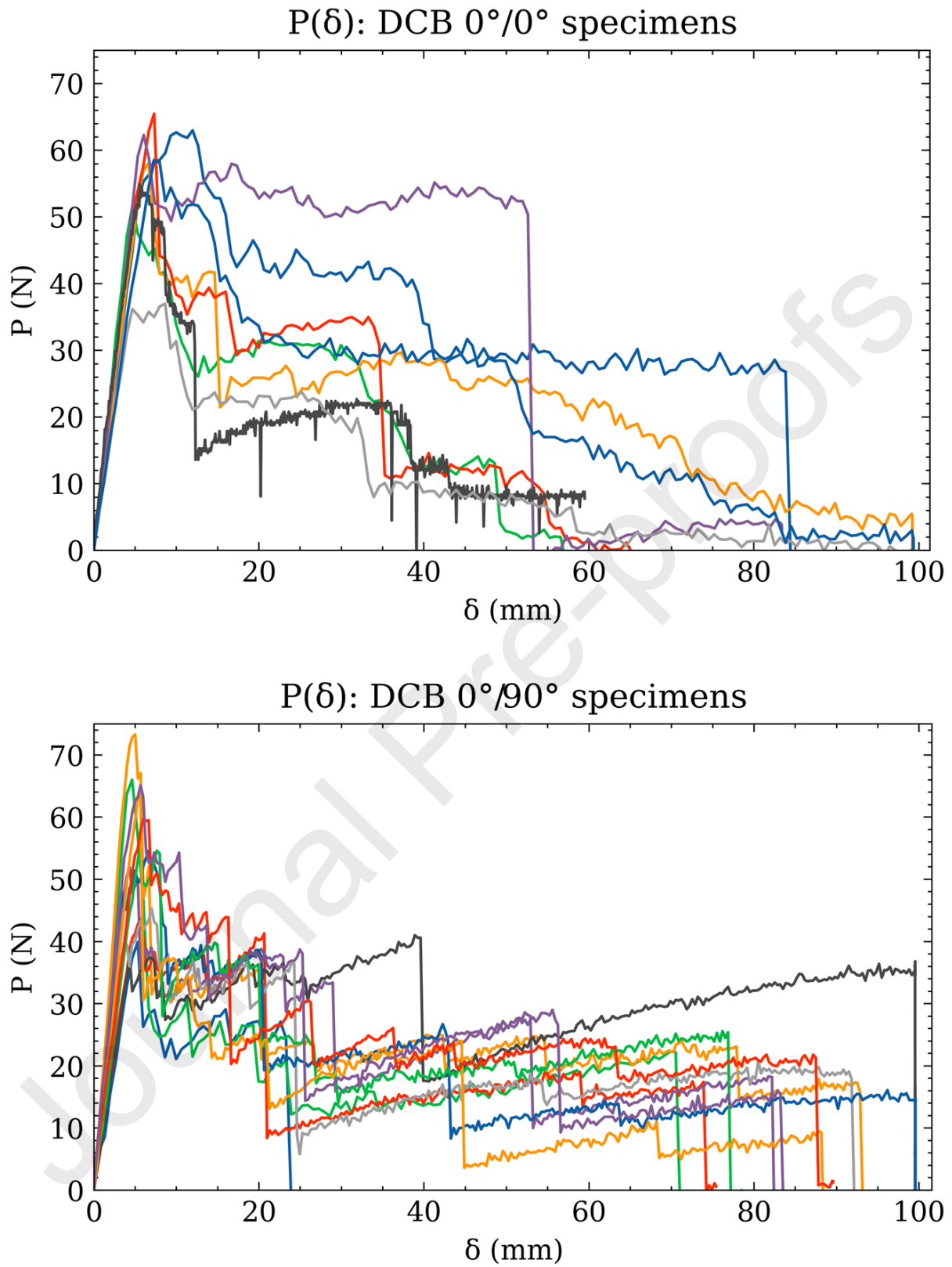


Figure 16- P - δ curves for $0^\circ/0^\circ$ specimens (top) and $0^\circ/90^\circ$ specimens (bottom)

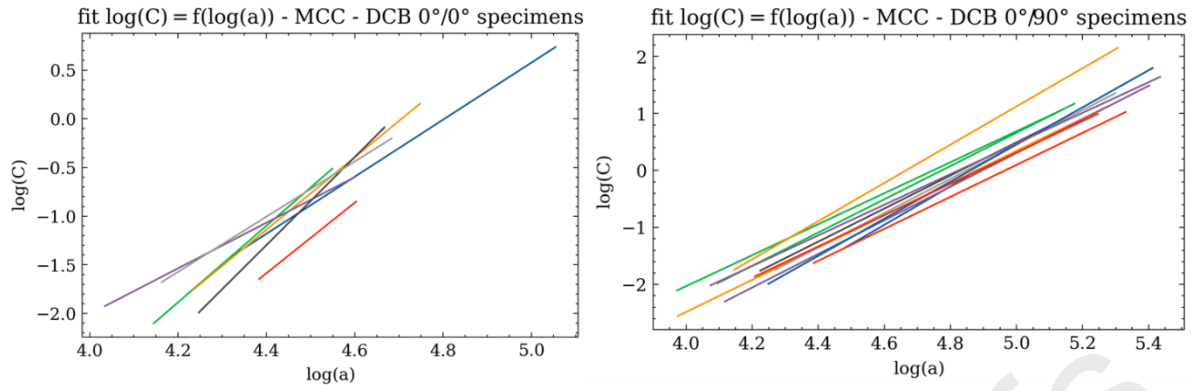


Figure 17 – Fit calibration with MCC method for 0°/0° specimens (left) and 0°/90° specimens (right)

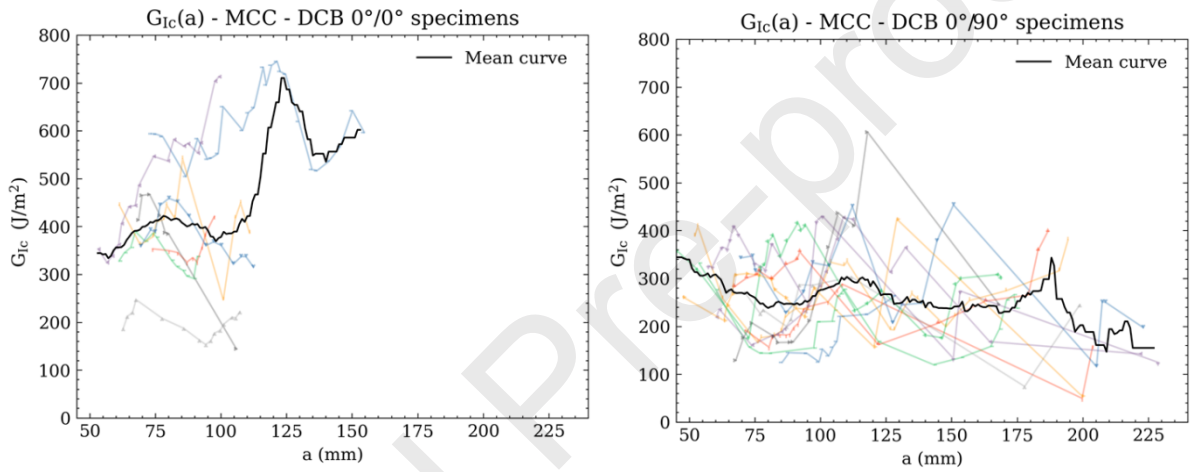


Figure 18 – R-curves for 0°/0° specimens (left) and 0°/90° specimens (right) with the mean curve (20-point rolling mean)

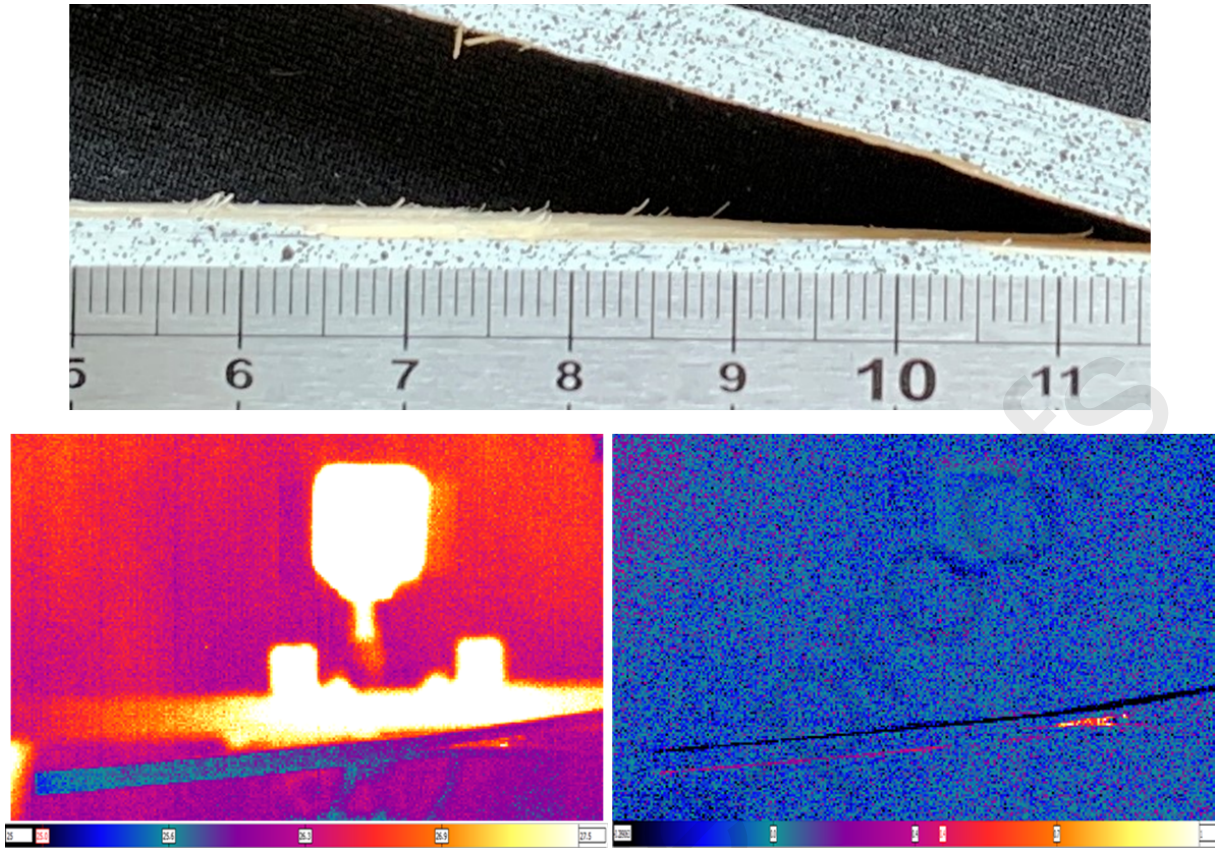


Figure 19 – Close-up view of broken fiber (top), IR camera capture (bottom left) and the difference between two consecutive images (bottom right)

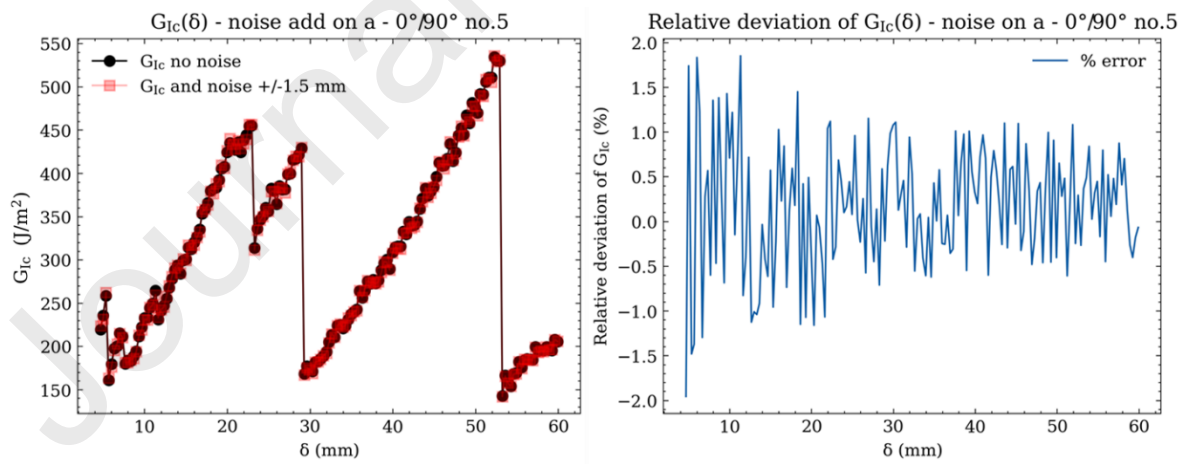


Figure 20 – G_{Ic} with and without noise added to the crack length measurement (left) and relative difference between G_{Ic} with and without noise added to the crack length measurement (right) on specimen 0°/90° no. 5

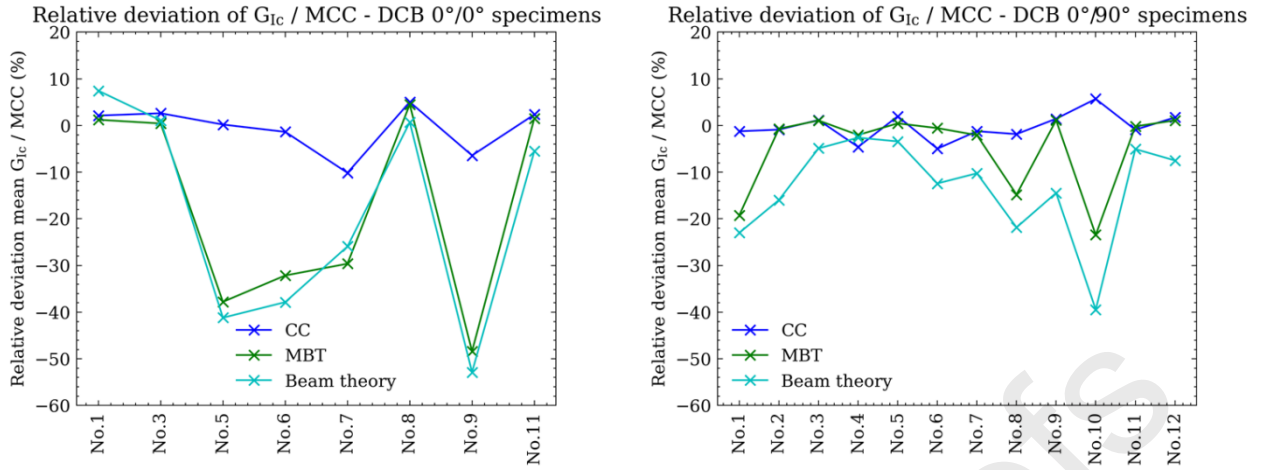


Figure 21 – Relative deviation of G_{Ic} methods compared to the MCC method for 0°/0° specimens (left) and 0°/90° specimens (right)

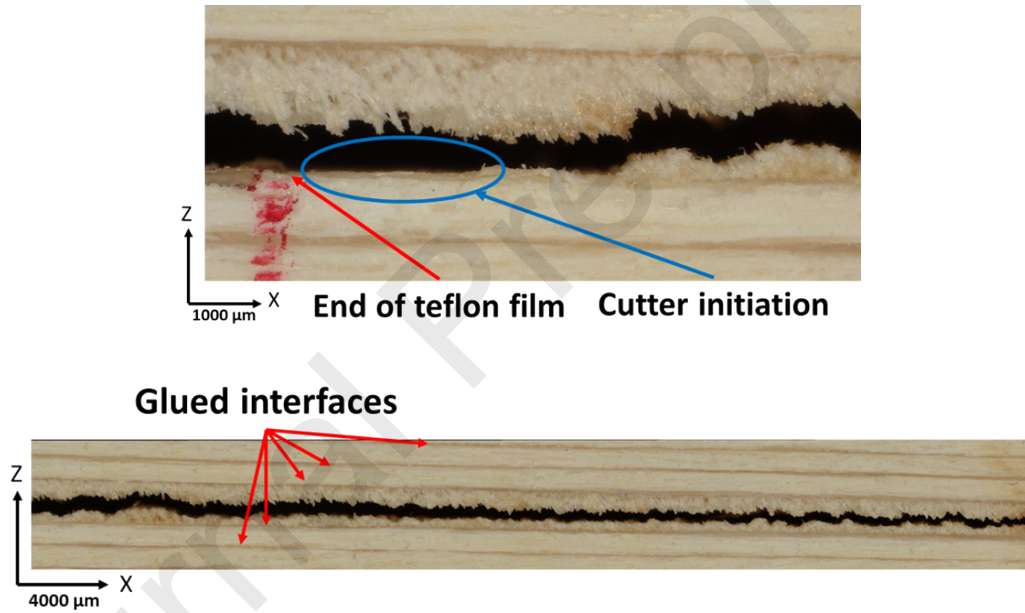


Figure 22 – Initiation and intra-ply migration (top) 90° ply; intra-ply crack propagation in 0°/90° specimen (bottom)

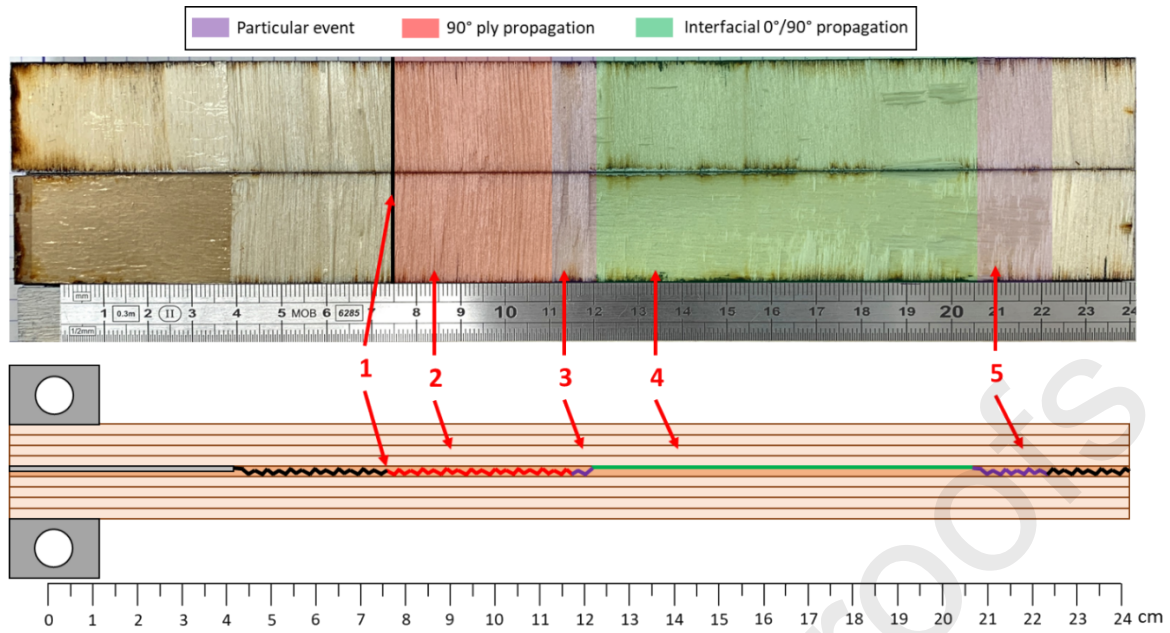


Figure 23 – Post-mortem examination of upper and lower interfaces of specimen 0°/90° no. 4 with identification of propagation zones (top) and illustration of the crack path and propagation zones through the same specimen (bottom) (*Colored figure*)

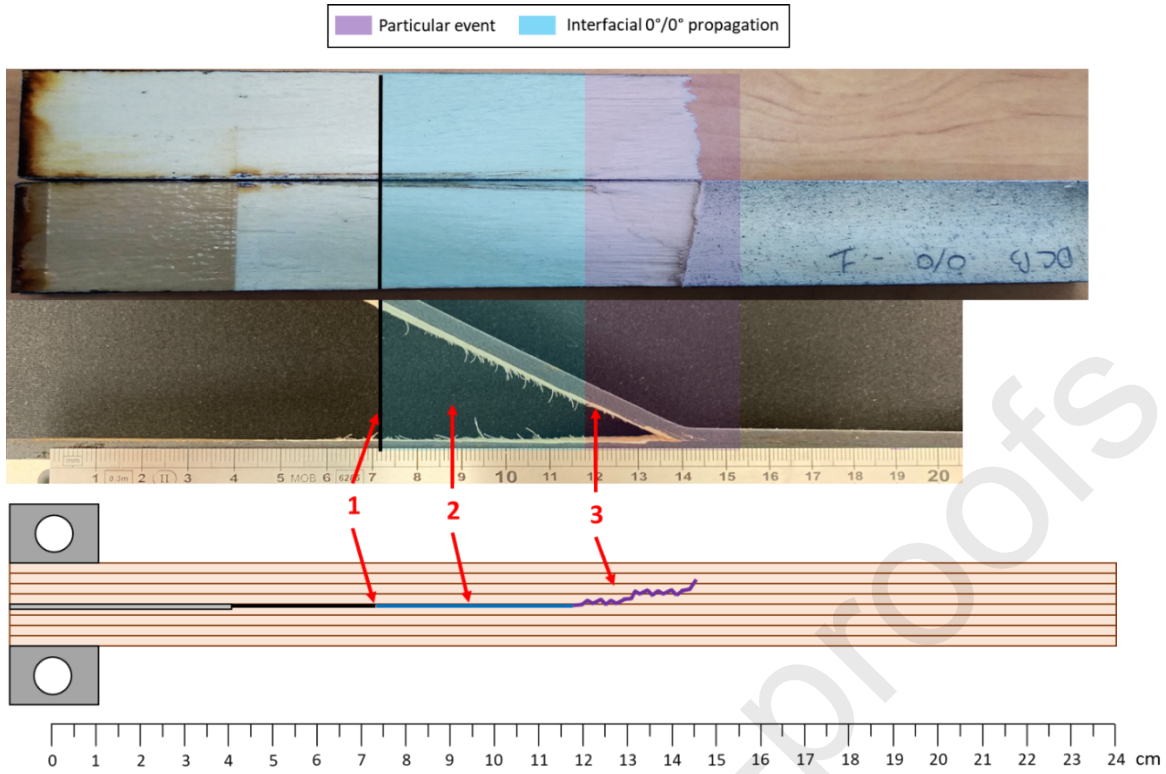


Figure 24 – Propagation zones (top) and illustration of the crack path (bottom) for the specimen

0°/0° no. 1 (Colored figure)

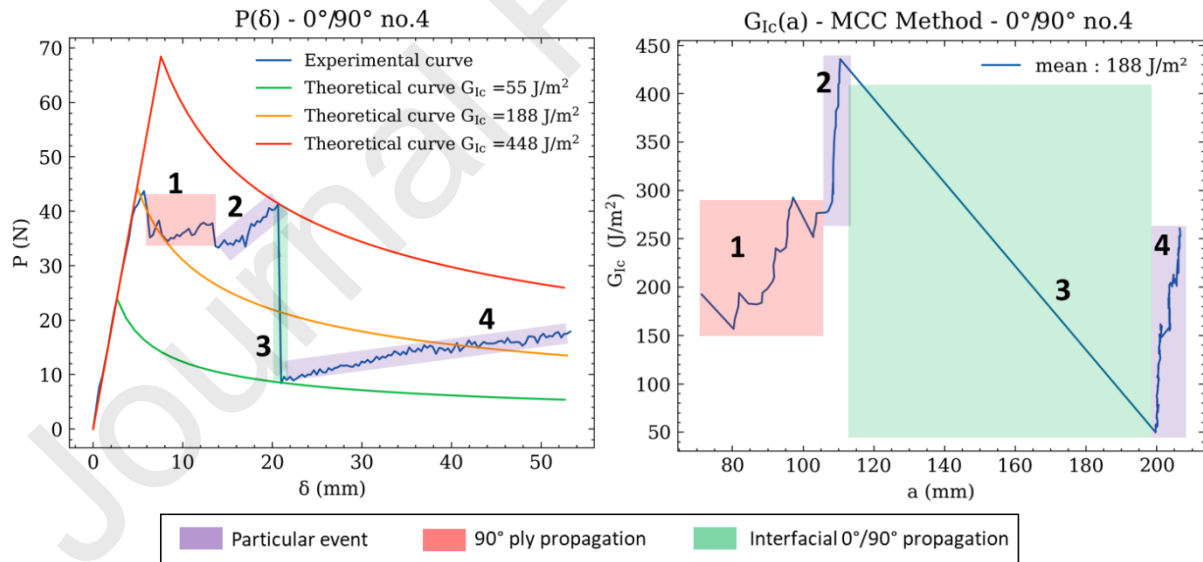


Figure 25 – Experimental and theoretical P-δ curves (left) and R-Curve (right) for the specimen

0°/90° no. 4 (Colored figure)

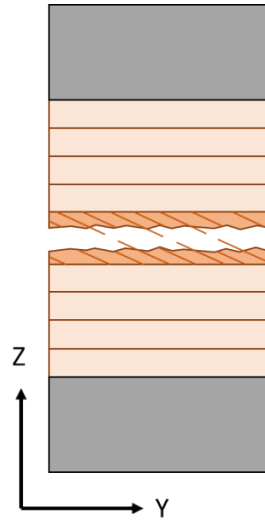


Figure 26 – Out-of-plane fiber bridging on 0°/90° specimens

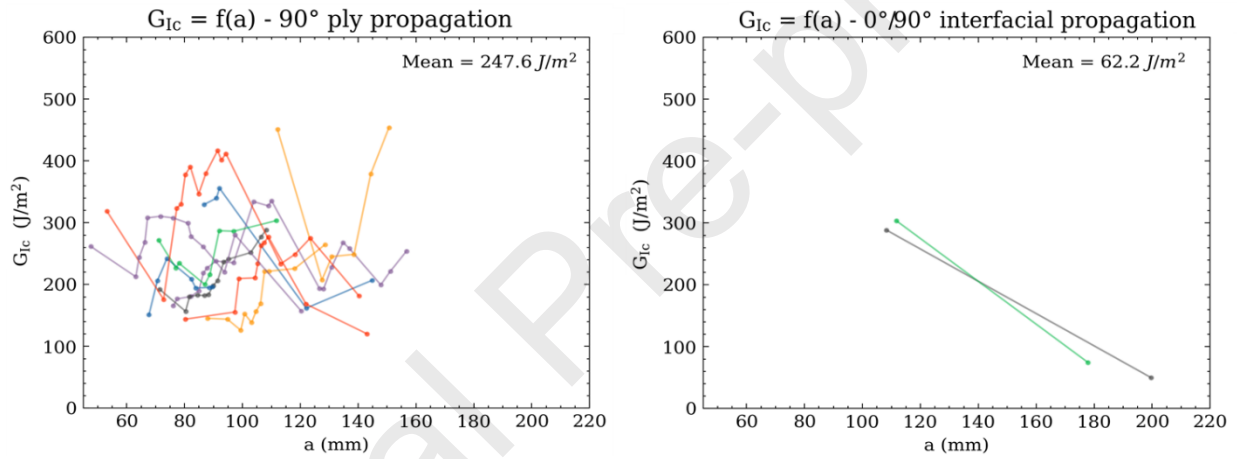


Figure 27 – $G_{Ic}=f(a)$ by propagation zones for 0°/90° specimens

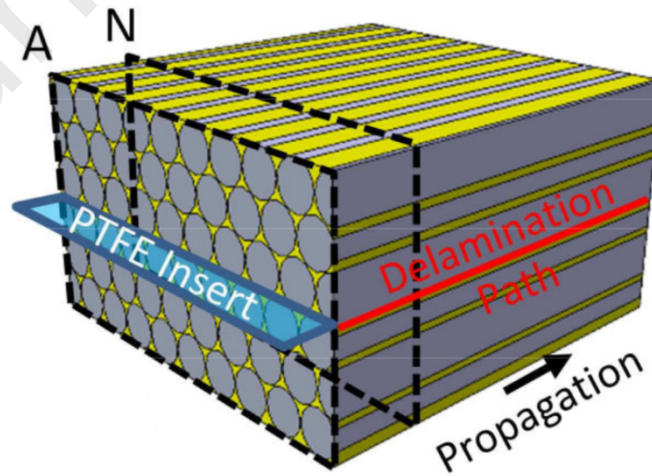


Figure 28 – Expected delamination path for a 0°/0° interface [50] (Colored figure)

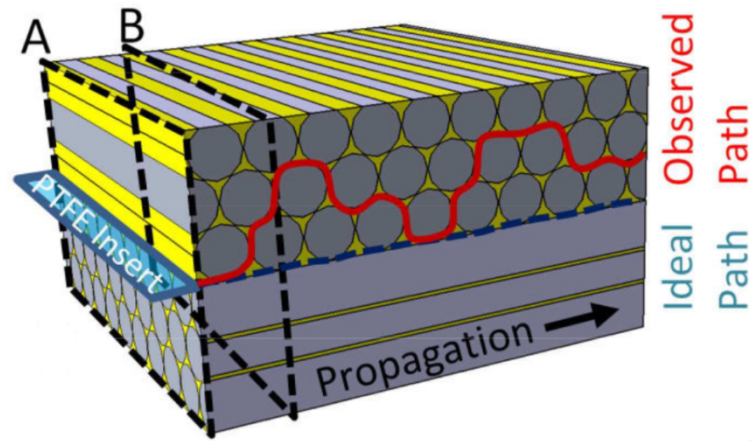


Figure 29 – Expected delamination path for a $0^\circ/90^\circ$ interface [50] (Colored figure)

Conflict of Interest Form

The authors declare that they have no known competing financial interests or personal relationships that could have appeared to influence the work reported in this paper.

Mode I delamination R-Curve in poplar laminated veneer lumber

A. Peignon¹, J. Serra¹, L. Gélard¹, A. Cantarel¹, F. Eyma¹ and B. Castanié^{1,*}

¹ Institut Clément (ICA), Université de Toulouse, CNRS UMR 5312, INSA, ISAE-Supaéro, INSA, IMT Mines Albi, UPS, Toulouse, France

*corresponding author: bruno.castanie@insa-toulouse.fr

Highlights:

- Mode I fracture toughness of laminated veneer lumber
- Characterization of 0°/0° and 0°/90° interfaces of laminated veneer lumber
- Fiber bridging and crack migration with double cantilever beam test
- Analyze of failure scenarios and patterns to compare 0°/0° and 0°/90° interfaces
- Digital image correlation used to track the crack propagation

Declaration of interests

☒ The authors declare that they have no known competing financial interests or personal relationships that could have appeared to influence the work reported in this paper.

☐ The authors declare the following financial interests/personal relationships which may be considered as potential competing interests:

A. Peignon, L. Gelard, F. Eyma, A. Cantarel, J. Serra, B. Castanié

Author Statement

Axel Peignon is the first author, responsible for sample preparation and testing, data analysis, and the preparation of the paper.

Joël Serra provided technical support in DCB testing, data analysis, and comments for the paper.

Léo Gélard was responsible for sample preparation and testing, and data analysis.

Florent Eyma and Arthur Cantarel provided technical guidance for the research and the preparation of the paper.

Bruno Castanié is the corresponding author and provided technical guidance for the research and the preparation of the paper